2SM

Observations: Atmosphere and Surface

Supplementary Material

Coordinating Lead Authors:
Dennis L. Hartmann (USA), Albert M.G. Klein Tank (Netherlands), Matilde Rusticucci (Argentina)

Lead Authors:
Lisa V. Alexander (Australia), Stefan Brönnimann (Switzerland), Yassine Abdul-Rahman Charabi (Oman), Frank J. Dentener (EU/Netherlands), Edward J. Dlugokencky (USA), David R. Easterling (USA), Alexey Kaplan (USA), Brian J. Soden (USA), Peter W. Thorne (USA/Norway/UK), Martin Wild (Switzerland), Panmao Zhai (China)

Contributing Authors:
Robert Adler (USA), Richard Allan (UK), Robert Allan (UK), Donald Blake (USA), Owen Cooper (USA), Aiguo Dai (USA), Robert Davis (USA), Sean Davis (USA), Markus Donat (Australia), Vitali Fioletov (Canada), Erich Fischer (Switzerland), Leopold Haimberger (Austria), Ben Ho (USA), John Kennedy (UK), Elizabeth Kent (UK), Stefan Kinne (Germany), James Kossin (USA), Norman Loeb (USA), Carl Mears (USA), Christopher Merchant (UK), Steve Montzka (USA), Colin Morice (UK), Cathrine Lund Myhre (Norway), Joel Norris (USA), David Parker (UK), Bill Randel (USA), Andreas Richter (Germany), Matthew Rigby (UK), Ben Santer (USA), Dian Seidel (USA), Tom Smith (USA), David Stephenson (UK), Ryan Teuling (Netherlands), Junhong Wang (USA), Xiaolan Wang (Canada), Ray Weiss (USA), Kate Willett (UK), Simon Wood (UK)

Review Editors:
Jim Hurrell (USA), Jose Marengo (Brazil), Fredolin Tangang (Malaysia), Pedro Viterbo (Portugal)

This chapter supplementary material should be cited as:
Hartmann, D.L., A.M.G. Klein Tank, M. Rusticucci, L. Alexander, S. Brönnimann, Y. Charabi, F. Dentener, E. Dlugokencky, D. Easterling, A. Kaplan, B. Soden, P. Thorne, M. Wild and P.M. Zhai, 2013: Observations: Atmosphere and Surface Supplementary Material. In: *Climate Change 2013: The Physical Science Basis. Contribution of Working Group I to the Fifth Assessment Report of the Intergovernmental Panel on Climate Change* [Stocker, T.F., D. Qin, G.-K. Plattner, M. Tignor, S.K. Allen, J. Boschung, A. Nauels, Y. Xia, V. Bex and P.M. Midgley (eds.)]. Available from www.climatechange2013.org and www.ipcc.ch.

Table of Contents

2.SM.1 Introduction

The Chapter 2 Supplementary Material includes data or methods for which there was not space in the printed document, but that are regarded as being valuable documentation for the main report or for subsequent scientific studies.

2.SM.2 Changes in Atmospheric Composition

2.SM.2.1 Long-Lived Greenhouse Gases

Table 2.SM.1 contains the full list of species compiled for Chapter 8 to use for radiative forcing calculations. Following are discussions of additional species not discussed in Section 2.2.1 of the main text.

2.SM.2.1.1 Hydrofluorocarbons

New measurements of several hydrofluorocarbons (HFCs) have been reported since AR4: HFC-365mfc (Stemmler et al., 2007), HFC-245fa (Vollmer et al., 2006), HFC-227ea (Laube et al., 2010) and HFC-236fa (Vollmer et al., 2011). Observation-based estimates of emissions show a mix of poor to good agreement with bottom-up inventories (Vollmer et al., 2011). Atmospheric abundances of these four minor HFCs were <2 ppt in 2011, but their atmospheric burdens are increasing rapidly, with relative increases >8% yr^{-1}.

2.SM.2.1.2 Perfluorocarbons

Atmospheric measurements of high molecular weight perfluorocarbons (PFCs) have also been reported, including fully fluorine-substituted alkanes (C_3 to C_8) (Saito et al., 2010; Ivy et al., 2012); and octafluorocyclobutane (c-C_4F_8) (Saito et al., 2010; Oram et al., 2012). All are currently <2 ppt, except when pollution events are observed at the air sampling sites.

2.SM.2.1.3 Nitrogen Trifluoride and Sulfuryl Fluoride

Since AR4, atmospheric observations of two new species were reported: NF_3 and SO_2F_2. Prather and Hsu (2008) reported the potential importance of NF_3 for radiative forcing. It is a substitute for PFCs as a plasma source in the semiconductor industry, has a lifetime of 500 years, and a GWP100 = 16,100 (GWPs are described in Chapter 8). Arnold et al. (2013) determined 0.59 ppt for its global annual mean mole fraction in 2008, growing from almost zero in 1978. In 2011, NF_3 was at 0.86 ppt, increasing by 0.49 ppt since 2005. Initial bottom-up inventories underestimated its emissions; based on the atmospheric observations, NF_3 emissions were 1.18 ± 0.21 Gg in 2011. SO_2F_2 replaces CH_3Br as a fumigant. Its GWP100 ≈ 4740, is comparable to CFC-11. A new estimate of its lifetime, 36 ± 11 year (Muhle et al., 2009), is significantly longer than previous estimates. Its global annual mean mole fraction in 2011 was 1.71 ppt and it increased by 0.36 ppt from 2005 to 2011.

2.SM.2.1.4 Halons

Atmospheric abundances of halons, except for halon-1301, have been decreasing. All have relatively small atmospheric abundances, ≤5 ppt, and are unlikely to accumulate to levels that can significantly affect radiative forcing either directly or indirectly through destruction of stratospheric ozone, if current emission projections are followed (WMO, 2011).

2.SM.2.2 Near-Term Climate Forcers

Figure 2.SM.1 shows ozone trends based on yearly average ozone values at the surface or within the lower troposphere beginning at different starting points since 1970. Most of the surface sites are in rural locations so that they are representative of regional air quality; however, many of the Asian sites are urban. Trend values are from the peer-reviewed literature listed in Table 2.SM.2.

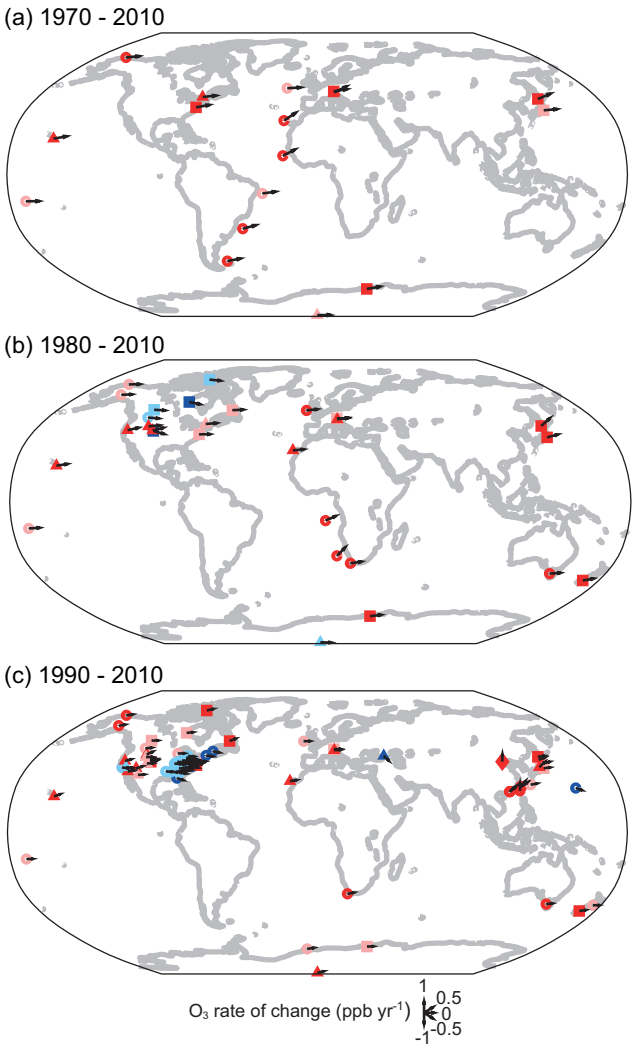

Figure 2.SM.1 | Ozone trends based on yearly average ozone values at the surface or within the lower troposphere (a) beginning between 1970 and 1979 and ending between 2000 and 2010. (b) Beginning between 1980 and 1989 and ending between 2000 and 2010 and (c) beginning between 1990 and 1999 and ending between 2000 and 2010. Measurements were made at the surface below 1 km (circles), at the surface above 1 km (triangles), in the lower troposphere by ozonesondes (squares) and in the lower troposphere by aircraft (diamonds). Vectors indicate the ozone rate of change as shown in the legend. Colors indicate ozone trends that are statistically significant and positive (red), statistically non-significant and positive (pink), statistically nonsignificant and negative (light blue) and statistically significant and negative (blue). Trend values are from the peer-reviewed literature listed in Table 2.SM.2.

Notes:

AGAGE = Advanced Global Atmospheric Gases Experiment; NOAA = National Oceanic and Atmospheric Administration, Earth System Research Laboratory, Global Monitoring Division; SIO = Scripps Institution of Oceanography, University of California, San Diego. CFC-11 = CCl_3F; CFC-113 = $CClF_2CCl_2F$; CFC-12 = CCl_2F_2; HCFC-22 = $CHClF_2$; HCFC-141b = CH_3CCl_2F; HCFC-142b = CH_3CClF_2; HFC-125 = CHF_2CF_3; HFC-134a = CH_2FCF_3; HFC-143a = CH_3CF_3; HFC-152a = CH_3CHF_2; HFC-23 = CHF_3, CFC-115 = $CClF_2CF_3$, H-1211 = $CBrClF_2$, H-1301 = $CBrF_3$, H-2402 = $CBrF_2CBrF_2$, HFC-227ea = CF_3CHFCF_3, HFC-236fa = $CF_3CH_2CF_3$, HFC-245fa = $CHF_2CH_2CF_3$, HFC-32 = CH_2F_2, HFC-365mfc = $CH_3CF_2CH_2CF_3$.

[a] Global surface annual mean dry-air mole fraction.

[b] Relative difference between AGAGE and NOAA 2011 global annual mean values (AGAGE – NOAA)/average).

[c] Source of data. Blank space indicated NOAA + AGAGE.

[d] Value listed from AGAGE data only, but NOAA maintains a scale and has unpublished data.

[e]

Table 2.SM.2 | Ozone trends reported in the literature, using data sets with at least 10 years of measurements. To understand ozone trends in air masses that are representative of regional or baseline conditions, measurements are from rural sites. However, in East Asia data are so limited that trends are also assessed in urban areas. Unless otherwise noted, trends are reported in ppb yr^{-1} with 95% confidence limits. Trends that are statistically significant at the 95% confidence level are shown in bold font. Trends are based on annual data unless seasons are specified. *Units are not listed for trend values reported in units of ppb yr^{-1}, but units are reported for trend values reported in percent per year.

Measurement Region	Site or Seasonal Information	Trend, ppb yr^{-1} (or percent per year)*	Period	Reference	Remarks
Europe					
Alpine high elevation surface sites, 3.0–3.6 km above sea level	A composite of Zugspitze, Jungfraujoch and Sonnblick	**0.87 ± 0.13** **0.33 ± 0.10** **–0.16 ± 0.14**	1978–1989 1990–1999 2000–2009	Logan et al. 2012)	Unfiltered data, although data from January to May, 1982 at Zugspitze were dropped. Quadratic fit to seasonal time series for 1978–2009.
Alpine high elevation surface site, 3.0 km above sea level	Zugspitze	**0.39 ± 0.06** **0.14 ± 0.06** 0.05 ± 0.08	1978–2010 1981–2010 1991–2010	Oltmans et al. (2013)	Annual trend is determined from monthly means using an autoregressive model that incorporates explanatory variables and a cubic polynomial fit.
Surface, rural central Europe	Hohenpeissenberg	**0.26 ± 0.07**	1971–2010	Parrish et al. (2012)	Filtered to remove very local contamination. The trend reported here is based on yearly averages and linear regression following the methods of Parrish et al. (2012).
Surface, west coast of Ireland	Mace Head	**0.31 ± 0.10**	1989–2010	Parrish et al. (2012)	See entry above. In addition the data were filtered to represent baseline transport conditions.
Surface, west coast of Ireland	Mace Head	**0.09 ± 0.08** 0.01 ± 0.10	1988–2010 1991–2010	Oltmans et al. (2013)	Daytime unfiltered data. Annual trend calculated from monthly means using an autoregressive model that incorporates explanatory variables and a cubic polynomial fit.
Surface, rural northern German coast	Arkona-Zingst	**0.32 ± 0.05**	1957–2010	Parrish et al. (2012)	Trend reported here is based on unfiltered yearly averages and linear regression following methods of Parrish et al. (2012).
Surface, alpine valley	Arosa	**0.40 ± 0.09**	1950–2000	Parrish et al. (2012)	See entry above. No measurements were made from the late 1950s through 1988.
Surface, rural elevated site in southeast Europe	Kislovodsk High Mountain Station	**–0.65 ± 0.01**	1991–2006	Tarasova et al. (2009)	Unfiltered data. Linear regression of all available hourly data.
Northern Europe mid-troposphere, 500 hPa	Composite of ozonesondes from Ny Alesund and Sodankyla	**0.25 ± 0.21**	1990–2006	Hess and Zbinden (2013)	Unfiltered data. Linear regression of 12-month running mean of monthly ozone deviations. This 17-year trend was calculated by P. Hess using the same method as for the 1990–2000 and 2000–2006 trends reported in the paper.
Central Europe lower free troposphere, 2.6–3.8 km above sea level	MOZAIC MOZAIC Hohenpeissenberg Payerne	0.15 ± 0.15 **–0.21 ± 0.20** **–0.20 ± 0.16** **–0.25 ± 0.17**	1995–2008 1998–2008 1998–2008 1998–2008	Logan et al. (2012)	Unfiltered data; see entry below. Trends at alpine sites for 1998–2008 show similar rates.
Central Europe mid- free troposphere, 5–6.1 km above sea level	MOZAIC MOZAIC Hohenpeissenberg Payerne	**0.33 ± 0.21** –0.08 ± 0.30 –0.1 ± 0.17 **–0.43 ± 0.19**	1995–2008 1998–2008 1998–2008 1998–2008	Logan et al. (2012)	Unfiltered data. Linear regression, with annual trend calculated from four seasonal trends; trends and annual cycle fit to monthly means. MOZAIC is a composite of aircraft flights to five European airports. Others are sonde stations.
North America					
Northeastern USA, rural mountaintop	Whiteface Mountain Summit, New York	**0.09 ± 0.06** 0.07 ± 0.08 **–0.22 ± 0.12**	1973–2010 1981–2010 1991–2010	Oltmans et al. (2013)	Annual trend is determined from monthly means using an autoregressive model that incorporates explanatory variables and a cubic polynomial fit.
Eastern USA, rural surface sites	Winter, 36 sites Spring, 40 sites Summer, 41 sites	0.12 (**44%, 0%**) –0.03 (**5%, 8%**) –0.45 (**0%, 66%**)	1990–2010	Cooper et al. (2012)	Mid-day data only. Linear regression of seasonal medians at a site. The reported trend is the average of the individual trends in the region. Values in parentheses indicate the percent of sites with statistically significant positive or negative trends, respectively.
Western USA, rural surface sites	Winter, 11 sites Spring, 12 sites Summer, 12 sites	0.12 (**36%, 0%**) 0.19 (**50%, 0%**) 0.10 (**17%, 8%**)	1990–2010	Cooper et al. (2012)	See entry above.
USA west coast, marine boundary layer	Composite of several sites	**0.27 ± 0.13**	1988–2010	Parrish et al. (2012)	Trend reported here is based on yearly averages and linear regression following methods of Parrish et al. (2012). Data were filtered to represent baseline transport conditions.
High latitudes, surface	Denali, central Alaska	0.04 ± 0.08 **0.15 ± 0.10**	1987–2010 1991–2010	Parrish et al. (2012)	Annual trend is determined from monthly means using an autoregressive model that incorporates explanatory variables and a cubic polynomial fit.
Arctic, surface	Barrow, Alaska	**0.09 ± 0.06** 0.03 ± 0.06 **0.13 ± 0.10**	1973–2010 1981–2010 1991–2010	Oltmans et al. (2013)	See entry above.
Eastern USA, free troposphere, 500 hPa	Annual composite of Wallops Island ozonesondes and MOZAIC aircraft profiles.	**0.41 ± 0.32**	1994–2006	Hess and Zbinden (2013)	Unfiltered data. Linear regression of annually averaged values for years when both ozonesonde and MOZAIC profiles were available. This 13-year trend was calculated by P. Hess using the same method as for the 1994–2000 and 2000–2006 trends reported in the paper.

Table 2.SM.2 (continued)

Measurement Region	Site or Seasonal Information	Trend, ppb yr^{-1} (or percent per year)*	Period	Reference	Remarks
Mid-Atlantic USA, coastal Virginia, surface–850 hPa	Wallops Island ozonesondes	**0.16 ± 0.12** 0.02 ± 0.16 **0.27 ± 0.22**	1971–2010 1981–2010 1991–2010	Oltmans et al. (2013)	Annual trend is determined from monthly means using an autoregressive model that incorporates explanatory variables and a cubic polynomial fit.
850–700 hPa	Wallops Island ozonesondes	0.08 ± 0.10 0.01 ± 0.12 **0.33 ± 0.14**	1971–2010 1981–2010 1991–2010	Oltmans et al. (2013)	See entry above.
700–500 hPa	Wallops Island ozonesondes	0.09 ± 0.10 0.01 ± 0.14 **0.27 ± 0.14**	1971–2010 1981–2010 1991–2010	Oltmans et al. (2013)	See entry above.
500–300 hPa	Wallops Island ozonesondes	–0.00 ± 0.18 0.20 ± 0.20 0.09 ± 0.32	1971–2010 1981–2010 1991–2010	Oltmans et al. (2013)	See entry above.
Western USA, surface–700 hPa	Boulder ozonesondes	**–0.24 ± 0.14** **0.19 ± 0.16**	1981–2010 1991–2010	Oltmans et al. (2013)	See entry above.
700–500 hPa	Boulder ozonesondes	**–0.36 ± 0.10** 0.06 ± 0.12	1981–2010 1991–2010	Oltmans et al. (2013)	See entry above.
500–300 hPa	Boulder ozonesondes	**–0.38 ± 0.18** 0.12 ± 0.26	1981–2010 1991–2010	Oltmans et al. (2013)	See entry above.
Eastern Canada, surface–850 hPa	Goose Bay ozonesondes	0.04 ± 0.10 **0.32 ± 0.12**	1981–2010 1991–2010	Oltmans et al. 2013)	See entry above.
850–700 hPa	Goose Bay ozonesondes	0.05 ± 0.12 **0.40 ± 0.16**	1981–2010 1991–2010	Oltmans et al. (2013)	See entry above.
700–500 hPa	Goose Bay ozonesondes	0.10 ± 0.12 **0.51 ± 0.16**	1981–2010 1991–2010	Oltmans et al. (2013)	See entry above.
500–300 hPa	Goose Bay ozonesondes	0.14 ± 0.28 **0.68 ± 0.32**	1981–2010 1991–2010	Oltmans et al. (2013)	See entry above.
Central Canada, surface–850 hPa	Churchill ozonesondes	**–0.18 ± 0.08** 0.09 ± 0.12	1981–2010 1991–2010	Oltmans et al. (2013)	See entry above.
850–700 hPa	Churchill ozonesondes	**–0.12 ± 0.10** 0.10 ± 0.16	1981–2010 1991–2010	Oltmans et al. (2013)	See entry above.
700–500 hPa	Churchill ozonesondes	–0.06 ± 0.10 **0.31 ± 0.16**	1981–2010 1991–2010	Oltmans et al. (2013)	See entry above.
500–300 hPa	Churchill ozonesondes	–0.05 ± 0.30 **0.55 ± 0.40**	1981–2010 1991–2010	Oltmans et al. (2013)	See entry above.
Western Canada, surface–850 hPa	Edmonton ozonesondes	–0.05 ± 0.10 0.02 ± 0.16	1981–2010 1991–2010	Oltmans et al. (2013)	See entry above.
850–700 hPa	Edmonton ozonesondes	**0.13 ± 0.10** **0.31 ± 0.12**	1981–2010 1991–2010	Oltmans et al. (2013)	See entry above.
700–500 hPa	Edmonton ozonesondes	**0.13 ± 0.10** **0.45 ± 0.12**	1981–2010 1991–2010	Oltmans et al. (2013)	See entry above.
500–300 hPa	Edmonton ozonesondes	**0.21 ± 0.20** **0.69 ± 0.26**	1981–2010 1991–2010	Oltmans et al. (2013)	See entry above.
Arctic Canada, surface–850 hPa	Resolute ozonesondes	–0.09 ± 0.12 **0.21 ± 0.16**	1981–2010 1991–2010	Oltmans et al. (2013)	See entry above.
850–700 hPa	Resolute ozonesondes	0.03 ± 0.12 **0.39 ± 0.18**	1981–2010 1991–2010	Oltmans et al. (2013)	See entry above.
700–500 hPa	Resolute ozonesondes	–0.00 ± 0.14 **0.40 ± 0.18**	1981–2010 1991–2010	Oltmans et al. (2013)	See entry above.
500–300 hPa	Resolute ozonesondes	0.00 ± 0.42 **1.17 ± 0.64**	1981–2010 1991–2010	Oltmans et al. (2013)	See entry above.
Western North America free troposphere (3–8 km)	Spring	**0.52 ± 0.20** **0.41 ± 0.27**	1984–2011 1995–2011	Cooper et al. (2012)	Unfiltered data. Linear regression based on median values of all available measurements (lidar, ozonesonde and aircraft) in the 3–8 km range during April to May.
Asia					
Mountaintop site in western Japan	Mt. Happo, 1.85 km above sea level	**0.65 ± 0.32**	1991–2011	Parrish et al. 2012)	Trend reported here is based on unfiltered yearly averages and linear regression following methods of Parrish et al., 2012.
Surface, rural eastern Japan	Ryori	0.22 ± 0.90	1991–2010	Oltmans et al. 2013)	Annual trend is determined from monthly means using an autoregressive model that incorporates explanatory variables and a cubic polynomial fit.

(continued on next page)

Table 2.SM.2 (continued)

Measurement Region	Site or Seasonal Information	Trend, ppb yr^{-1} (or percent per year)*	Period	Reference	Remarks
Japanese marine boundary layer	Composite of 3 sites in western Japan	0.31 ± 0.34	1998–2011	Parrish et al. 2012)	Trend reported here is based on unfiltered yearly averages & linear regression following methods of Parrish et al., 2012.
Beijing, China, boundary layer	Annual Summer afternoons	**~1** **~3**	1997–2004	Ding et al. 2008)	The rate of change was derived from a comparison of mean MOZAIC aircraft profiles during the periods 1995–1999 and 2000–2005.
Northern Taiwan, China, elevated surface site	YangMing	**0.54 ± 0.2**1	1994–2007	Lin et al. 2010)	Unfiltered data. Linear regression of annual means, using data from all times of day.
Taiwan, China Surface	Composite of 3 coastal sites near urban emissions.	**0.52 ± 0.10**	1994–2007	Lin et al. 2010)	Unfiltered data. Linear regression of annual means, using data from all times of day.
Taiwan, China surface	Composite of 12 urban sites in the north of the country.	**0.75 ± 0.07**	1994–2007	Lin et al. 2010)	Unfiltered data. Linear regression of annual means, using data from all times of day.
Taiwan, China, surface	Composite of 4 sites in southern Taiwan, near urban emissions.	~1.5	1997–2006	Li et al. 2010)	Unfiltered data. Linear regression using monthly means. The reported trend was inferred from the regression line in Figure 2. Significance at the 95% confidence limit was not specified.
Hong Kong, surface	Hok Tsui coastal site on southern tip of Hong Kong Island	**0.58**	1994–2007	Wang et al. 2009b)	Unfiltered data. Linear regression of monthly means, using all months and all times of day. This site is often upwind of the Hong Kong urban area.
Northern Japan, surface–850 hPa	Sapporo ozonesondes	**0.35 ± 0.10** **0.63 ± 0.12** **0.15 ± 0.14**	1971–2010 1981–2010 1991–2010	Oltmans et al. 2013)	Annual trend is determined from monthly means using an autoregressive model that incorporates explanatory variables and a cubic polynomial fit.
850–700 hPa	Sapporo ozonesondes	**0.23 ± 0.10** **0.48 ± 0.12** –0.02 ± 0.12	1971–2010 1981–2010 1991–2010	Oltmans et al. 2013)	See entry above
700–500 hPa	Sapporo ozonesondes	**0.23 ± 0.10** **0.38 ± 0.12** 0.07 ± 0.14	1971–2010 1981–2010 1991–2010	Oltmans et al. 2013)	See entry above
500–300 hPa	Sapporo ozonesondes	0.16 ± 0.20 0.10 ± 0.20 –0.03 ± 0.28	1971–2010 1981–2010 1991–2010	Oltmans et al. 2013)	See entry above
Central Japan, surface–850 hPa	Tsukuba ozonesondes	0.08 ± 0.14 **0.23 ± 0.22** 0.09 ± 0.30	1971–2010 1981–2010 1991–2010	Oltmans et al. 2013)	See entry above
850–700 hPa	Tsukuba ozonesondes	**0.16 ± 0.12** **0.21 ± 0.16** 0.09 ± 0.24	1971–2010 1981–2010 1991–2010	Oltmans et al. 2013)	See entry above
700–500 hPa	Tsukuba ozonesondes	**0.16 ± 0.10** **0.23 ± 0.14** **0.21 ± 0.20**	1971–2010 1981–2010 1991–2010	Oltmans et al. 2013)	See entry above
500–300 hPa	Tsukuba ozonesondes	**0.34 ± 0.20** **0.41 ± 0.26** 0.92 ± 1.12	1971–2010 1981–2010 1991–2010	Oltmans et al. 2013)	See entry above
Southern Japan, surface–850 hPa	Naha ozonesondes	0.17 ± 0.20	1991–2010	Oltmans et al. 2013)	See entry above
850–700 hPa	Naha ozonesondes	0.09 ± 0.20	1991–2010	Oltmans et al. 2013)	See entry above
700–500 hPa	Naha ozonesondes	**0.21 ± 0.20**	1991–2010	Oltmans et al. 2013)	See entry above
500–300 hPa	Naha ozonesondes	0.22 ± 0.22	1991–2010	Oltmans et al. 2013)	See entry above
South Asia, tropospheric column ozone as measured by satellites	A broad region including much of India, southeast Asia and Indonesia	**0.3–0.7 % yr^{-1}**	1979–2005	Beig and Singh, 2007)	The decadal trend was calculated using a multifunctional regression model. Here the trend is converted to percent yr^{-1}.
North Pacific Ocean tropics and subtropics					
Minamitorishima, Japan	Remote Japanese island 4000 km east of southern China	**–0.29 ± 0.14**	1994–2010	Oltmans et al. 2013)	Annual trend is determined from monthly means using an autoregressive model that incorporates explanatory variables and a cubic polynomial fit.
Mauna Loa, Hawaii	3.4 km above sea level	**0.16 ± 0.08** **0.14 ± 0.08** **0.31 ± 0.14**	1974–2010 1981–2010 1991–2010	Oltmans et al. 2013)	See entry above. Only night time data were used to ensure downslope flow conditions.

(continued on next page)

Table 2.SM.2 (continued)

Measurement Region	Site or Seasonal Information	Trend, ppb yr^{-1} (or percent per year)*	Period	Reference	Remarks
Hawaii, USA surface–850 hPa	Hilo ozonesondes	**–0.38 ± 0.16** **0.25 ± 0.18**	1982–2010 1991–2010	Oltmans et al. 2013)	See entry above
850–700 hPa	Hilo ozonesondes	0.04 ± 0.16 0.15 ± 0.22	1982–2010 1991–2010	Oltmans et al. 2013)	See entry above
700–500 hPa	Hilo ozonesondes	0.11 ± 0.16 0.14 ± 0.24	1982–2010 1991–2010	Oltmans et al. 2013)	See entry above
500–300 hPa	Hilo ozonesondes	0.09 ± 0.16 0.05 ± 0.26	1982–2010 1991–2010	Oltmans et al. 2013)	See entry above
Northern Hemisphere Atlantic Ocean					
Marine boundary layer, eastern North Atlantic Ocean	40°N–60°N 20°N–40°N 0°–20°N	0.05 **0.51** **0.42**	1977–2002	Lelieveld et al. 2004)	Unfiltered measurements from ships traversing the indicated regions. The 95% confidence limits were not reported, although statistical significance was.
Marine boundary layer, western North Atlantic Ocean	Bermuda	**0.31 ± 0.25** (winter) 0.27 ± 0.29 (spring) **0.30 ± 0.16** (summer) 0.05 ± 0.33 (autumn)	1989–2010	Parrish et al. 2012)	Unfiltered data. Linear regression of seasonal averages. There is a data gap of 5 years in the middle of the record.
Canary Islands, subtropical marine location west of North Africa	Izana, Tenerife, 2800 m above sea level.	**0.14 ± 0.10**	1991–2010	Oltmans et al. 2013)	Annual trend is determined from monthly means using an autoregressive model that incorporates explanatory variables and a cubic polynomial fit. Only night time data were used to ensure downslope flow conditions.
Northern Hemisphere upper troposphere		Seasons with a significant increase in ozone			
Western USA Northeast USA N. Atlantic Ocean Europe Middle East Northern India South China Northern Japan Southern Japan		None **Winter, spring** **Winter** **Spring** **Spring, summer** **Spring, summer** **Summer** **Summer, autumn** **All seasons**	Ozone change between 1975–1979 and 1994–2001	Schnadt Poberaj et al. 2009)	Ozone changes were calculated for various regions of the northern hemisphere upper troposphere that were sampled by the NASA GASP aircraft program in the 1970s and by the European MOZAIC program in the 1990s. No region had a statistically significant decrease in ozone, in any season.
Southern Hemisphere					
Tropical South Pacific Ocean, marine boundary layer	Samoa	0.01 ± 0.04 **0.05 ± 0.04** 0.02 ± 0.68	1976–2010 1981–2010 1991–2010	Oltmans et al. 2013)	Annual trend is determined from monthly means using an autoregressive model that incorporates explanatory variables and a cubic polynomial fit.
Marine boundary layer, western South Atlantic Ocean	40°S–60°S 20°S–40°S 0°S–20°S	**0.17** **0.24** 0.12	1977–2002	Lelieveld et al. 2004)	Unfiltered measurements from ships traversing the indicated regions. The 95% confidence limits were not reported, although statistical significance was.
Marine boundary layer, eastern South Atlantic Ocean	20°S–40°S 0°–20°S	**0.68** **0.37**	1977–2002	Lelieveld et al. 2004)	See entry above
Mid-latitude marine boundary layer	Cape Point, South Africa	**0.13 ± 0.02** **0.17 ± 0.04**	1983–2010 1991–2010	Oltmans et al. 2013)	Annual trend is determined from monthly means using an autoregressive model that incorporates explanatory variables and a cubic polynomial fit.
Mid-latitude marine boundary layer	Cape Grim, Tasmania, Australia	**0.06 ± 0.02** **0.09 ± 0.04**	1982–2010 1991–2010	Oltmans et al. 2013)	See entry above
Mid-latitude rural coastal site	Baring Head, New Zealand	0.01 ± 0.06	1991–2010	Oltmans et al. 2013)	See entry above
Antarctica, Ekström ice shelf, 10 km from the ocean	Neumayer	0.13 ± 0.16	1995–2005	Helmig et al. 2007)	Unfiltered data. Linear regression based on annual median values.
Antarctica, 2.8 km above sea level	South Pole	0.01 ± 0.04 –0.01 ± 0.41 **0.20 ± 0.04**	1975–2010 1981–2010 1991–2010	Oltmans et al. 2013)	Annual trend is determined from monthly means using an autoregressive model that incorporates explanatory variables and a cubic polynomial fit.
Tropical Indian Ocean, La Reunion Island ozonesonde profiles	2–4 km a.s.l 4–10 km a.s.l. 10–16 km a.s.l.	0.01 ± 0.69 % yr^{-1} 0.44 ± 0.58 % yr^{-1} **1.23 ± 0.58 % yr^{-1}**	1992–2008	Clain et al. 2009)	Unfiltered ozonesonde measurements. Linear regression of all available year-round measurements.
Subtropical South Africa, Irene ozonesonde profiles	2–4 km a.s.l 4–10 km a.s.l. 10–16 km a.s.l.	**1.44 ± 0.40 % yr^{-1}** **0.40 ± 0.33 % yr^{-1}** 0.19 ± 0.35 % yr^{-1}	1990–2008	Clain et al. 2009)	Unfiltered ozonesonde measurements. Linear regression of all available year-round measurements. No data for 1994–1997.
Southern New Zealand surface–850 hPa	Lauder, ozonesondes	**0.15 ± 0.06** **0.12 ± 0.08**	1986–2010 1991–2010	Oltmans et al. 2013)	Annual trend is determined from monthly means using an autoregressive model that incorporates explanatory variables and a cubic polynomial fit.

(continued on next page)

Table 2.SM.2 (continued)

Measurement Region	Site or Seasonal Information	Trend, ppb yr^{-1} (or percent per year)*	Period	Reference	Remarks
850–700 hPa	Lauder, ozonesondes	**0.14 ± 0.06** **0.10 ± 0.06**	1986–2010 1991–2010	Oltmans et al. 2013)	See entry above
700–500 hPa	Lauder, ozonesondes	**0.16 ± 0.08** **0.20 ± 0.08**	1986–2010 1991–2010	Oltmans et al. 2013)	See entry above
500–300 hPa	Lauder, ozonesondes	0.06 ± 0.12 0.12 ± 0.14	1986–2010 1991–2010	Oltmans et al. 2013)	See entry above
Coastal Antarctica, surface–850 hPa	Syowa, ozonesondes	**0.15 ± 0.06** **0.10 ± 0.06** 0.02 ± 0.08	1971–2010 1981–2010 1991–2010	Oltmans et al. 2013)	See entry above
850–700 hPa	Syowa, ozonesondes	0.06 ± 0.06 0.03 ± 0.06 0.06 ± 0.06	1971–2010 1981–2010 1991–2010	Oltmans et al. 2013)	See entry above
700–500 hPa	Syowa, ozonesondes	**0.05 ± 0.04** 0.01 ± 0.06 **0.12 ± 0.08**	1971–2010 1981–2010 1991–2010	Oltmans et al. 2013)	See entry above
500–300 hPa	Syowa, ozonesondes	–0.10 ± 0.10 –0.07 ± 0.14 0.18 ± 0.16	1971–2010 1981–2010 1991–2010	Oltmans et al. 2013)	See entry above
Central Antarctica, 700–500 hPa	South Pole, ozonesondes	**0.05 ± 0.04** **0.08 ± 0.06**	1986–2010 1991–2010	Oltmans et al. 2013)	See entry above
500–300 hPa	South Pole, ozonesondes	0.12 ± 0.14 0.09 ± 0.18	1986–2010 1991–2010	Oltmans et al. 2013)	See entry above

2.SM.2.3 Aerosols

Comprehensive, long-term and high-quality observations of aerosols were initiated mainly after 2000, and are currently available only at a few locations and regions. The monitoring and observations of aerosols are still to a large degree uncoordinated on the continental and global scale, despite the crucial importance of aerosols as short-lived climate forcers. A few long-term background measurements of aerosol properties are performed within the framework of WMO GAW (World Meteorological Organisation Global Atmosphere Watch program); however, the data coverage is low. An overview and critical evaluation of worldwide, quality assured, aerosol trend measurements does not exist at present. For studies of aerosol–climate interactions, it is crucial that the sites are representative for regional/rural conditions, with low influence of local pollution and that the measurements are harmonised among sites and networks, and provided as homogeneous time series.

Regional air pollution networks in Europe and North America are the most reliable source of information on long-term surface aerosol trends in these parts of the world. In Europe, the European Monitoring and Evaluation Programme (EMEP) network provides regionally representative measurements of aerosol composition since the 1980s; these measurements are described in annual reports, and they are available via www.emep.int. Torseth et al. (2012) provide an overview of results from two or three decades of EMEP measurements, as discussed in Section 2.2.3.

In North America, the U.S. Clean Air Status and Trends Network (CASTNET) and the Canadian Air and Precipitation Monitoring Network (CAPMoN) provide regionally representative long-term measurements of major ions in aerosols, including sulphate (Hidy and Pennell, 2010); these networks do not report $PM_{2.5}$. The U.S. Interagency Monitoring of Protected Visual Environments (IMPROVE) Network has measured $PM_{2.5}$ and PM_{10} (particulate matter with aerodynamic diameters <2.5 and <10 µm, respectively) mass, total aerosol composition and visibility at about 60 regional stations since 1989 (Hand et al., 2011). Canadian CAPMoN network results are summarized in Canada (2012).

In Asia, the Acid Deposition Network East Asia (EANET, 2011) has measured particulate matter and deposition since 2001, but thus far no trend studies have been published. In China, CAWNET (China Atmosphere Watch Network) and CARSNET (Calibration campaign of the China Aerosol Remote Sensing NETwork) recently began systematic aerosol observations (Zhang et al., 2012); however, only a few years of data are available. An analysis of population weighted $PM_{2.5}$ measurements reported in Brauer et al. (2012) showed that China has the worlds highest average $PM_{2.5}$ (55 µg m^{-3}), more than twice the global average, indicating a strong influence of pollutant emissions. An analysis (Qu et al., 2010) of reconstructed urban PM_{10} time series (2000–2006) from reported air pollution indices in 86 Chinese cities suggests that median aerosol concentrations declined from 108 to 95 µg m^{-3} in 16 northern cities and increased slightly from 52 to 60 µg m^{-3} in 12 southern cities. Quan et al. (2011) report strong declines in visibility commencing in the 1970s in the eastern provinces of China, and continuing through the 2000s. They link these reduced visibility levels to emission changes and high PM levels. See the discussion of visibility measurements in Section 2.2.3.1 and in Wang et al. (2009a, 2012).

In some other Asian regions long-term measurements from individual research groups or small networks are becoming available, but it is often difficult to assess the significance of these measurements for larger regions.

In India, the Central Pollution Control Board (CPCB), Government of India, is executing a nation-wide programme of ambient air quality

monitoring known as the National Air Quality Monitoring Programme (NAMP). The network consists of 342 monitoring stations covering 127 cities/towns in 26 States and 4 Union Territories. The State of Environment Report (Ministery of Environment and Forest, 2009) reported annual average levels of respirable particulate matter (approximately PM_{10}) in residential areas of major cities ranging from 120 to 160 µg m^{-3} (Delhi), 80 to 120 µg m^{-3} (Mumbai), 30 to 90 µg m^{-3} (Chennai), and 120 to 140 µg m^{-3} (Kolkata); in these cities' trends are mostly stable or increasing for 2000–2007. No details on the robustness of trends are given, and the validity of these trends for rural regions is not reported.

Surface-based remote sensing of aerosols, as discussed in Section 2.2.3.1, is based mainly on results from the global AERONET network (Holben et al., 1998). However, coverage of AERONET over several regions is poor. Since AR4, several other regional networks were established such as ARFINET covering India(Krishna Moorthy et al., 2013); AEROCAN over Canada (http://www.aerocanonline.com/), and SKYNET over Japan (Kim et al., 2004); these data are not included in this analysis.

2.SM.2.3.1 North American Sulphate Trends

In Section 2.2.3.2 overall declines of SO_4^{2-} from the IMPROVE (Hand et al., 2011) network are on the order of 2 to 4% yr^{-1}, but slightly larger (about 6% yr^{-1}) along the east coast of the USA. SO_4^{2-} declines in winter were somewhat larger than in other seasons. These trends are consistent with average trends reported by CASTNET (2010) of –0.045 µg S m^{-3} yr^{-1} for the period 1990–2008 in the eastern US, and a decrease of CASTNET aerosol sulphate concentrations by –21% in the East and Northeast, –22% in the Midwest, and –20% in the South between the two periods 1990–1994 and 2000–2004 (Sickles and Shadwick, 2007a). Indirect evidence for declining sulphate particulate concentrations is found in an analysis of SO_4^{2-} wet deposition by 20 to 30% over a time period of 15 years (Sickles and Shadwick, 2007b), corresponding to a trend of about –1.4 to –2.1% yr^{-1}. In Canada, aerosol sulphate concentrations declined by 30 to 45% between 1991–1993 and 2004–2006 at non-urban CAPMoN sites in the eastern half of the country. These declines are consistent with the trends of inorganic aerosol components reported by Quinn et al. (2009) at Barrow, Alaska, ranging between –2.3% yr^{-1} for SO_4^{2-} to –6.4% for NH_4. Hidy and Pennell (2010) show remarkable agreement of $PM_{2.5}$ and SO_4^{2-} declines in Canada, pointing to common emission sources of $PM_{2.5}$ and SO_4^{2-}.

2.SM.2.3.2 Black (Light Absorbing) and Elemental Carbon Trends

The terms black carbon (BC), also referred to as light absorbing carbon (LAC), and elemental carbon (EC) refer to the analysis method: optical methods (aerosol light absorption) or filter measurements using thermal methods, respectively. For a detailed discussion on methods, see Bond et al. (2013). The measurements are associated with large uncertainties; intercomparisons show differences of a factor of 2 to 3 for optical methods, and a factor of 4 for thermal methods (Vignati et al., 2010) which also renders quantitative comparison of LAC time series uncertain. In addition, although there is a general lack of BC/EC measurements, long-term time series are even scarcer.

In Europe, long-term EC and organic carbon (OC) data have been available at two stations (in Norway and Italy) starting in 2001 (Yttri et al., 2011). Torseth et al. (2012) report slight decreases over these 9 years, but with no assessment of statistical significance. In North America, the combined IMPROVE and CSN network (Hand et al., 2011) is measuring elemental and organic carbon. However, trend analysis of long-term data are reported only (Hand et al., 2011) for total carbon (TC = black carbon + organic carbon), as an upgrade in sampling techniques around 2005 led to a different measured ratio of EC and OC. These TC measurements indicate highly significant (95% confidence) downward trends of total carbon between 2.5 and 7.5% yr^{-1} along the east and west coasts of the USA, and smaller and less significant ($p < 0.15$) trends in other USA regions from 1989 to 2008. Sharma et al. (2006) published long-term measurements of equivalent BC at Alert, Canada and Barrow, Alaska, USA. Decreases were 54% at Alert and 27% at Barrow for 1989–2003; part of the trend difference was associated with changes in circulation patterns, that is, the phase of North Atlantic Oscillation (NAO).

In China, constant EC concentrations until the late 1970s have been derived from sediments at Chaohu and Lake Taihu in Eastern China (Han et al., 2011), followed by a sharp increase afterwards, corresponding to the rapid industrialization of China in the last three decades. An analysis of broadband radiometer data from 1957 to 2007 (Wang and Shi, 2010) showed a slight decrease in absorption of aerosol after 1990, likely due to LAC, while there was no significant change in the scattering fraction of aerosol.

In India, downward trends in BC of 250 ng m^{-3} yr^{-1} (from 4000 to 2000 ng m^{-3}) in the period 2001–2009 were observed at the southern station of Trivandrum, with the largest changes occurring in 2007–2009 (Krishna Moorthy et al., 2009). At the northern Kanpur station increases of Aerosol Optical Depth (AOD) during the post-monsoon period and winter were observed for 2001–2010, attributed to anthropogenic emission changes, with declining trends during the pre-monsoon and monsoon seasons, attributed to changes in natural emissions (Kaskaoutis et al., 2012).

2.SM.2.4 Carbon Monoxide Surface Measurements

Analysis of carbon monoxide (CO) data from the NOAA ESRL GMD global cooperative air sampling network (data path: ftp://ftp.cmdl.noaa.gov/ccg/co/flask/) indicates a small decrease in globally averaged CO from 2006 to 2010. These findings are corroborated by analysis of 1994–2012 AGAGE baseline CO measurements at Mace Head, Ireland (updated from Prinn et al. (2000), http://agage.eas.gatech.edu/data.htm) which showed large variability until 2005, and smaller variability together with stable or slightly decreasing CO from 2006–2012. The observations are consistent with estimates of a slight decline in global anthropogenic CO emissions over the same time, although East Asian emissions may have increased (Granier et al., 2011).

2.SM.3 Quantifying Changes in the Mean: Trend Models and Estimation in Box 2.2

The Supplementary Material provides a detailed description of the method used to estimate linear trends in Chapter 2 and compares the

results of this relatively simple method with those of a wide variety of other methods for fitting lines to data and estimating their uncertainty. It is demonstrated that the differences among the methods are rather small compared to the uncertainty estimates of each method. Details of the smoothing method used to produce the result shown in Box 2.2, Figure 1, are also provided.

2.SM.3.1 Methods of Estimating Linear Trends and Uncertainties

Several different methods of calculating linear trends and their uncertainties are illustrated here by application to the annual mean time series of globally averaged Earth surface temperatures from the HadCRUT4 data set (see Section 2.4.3 for details). The methods used are described briefly below. The conclusion of this analysis is that, for time series like the one used here, the trend line slope and its uncertainty limits are very similar for most of the methods that take into account dependency in the data sets in the form of the first-order autoregressive model AR(1). These results are similar to those obtained by the Restricted Maximum Likelihood (REML) method used in AR4. The similarity of the AR4 method results to those of the methods investigated here was determined by applying these methods to AR4 data sets and obtaining similar results for linear trends and their uncertainties (not shown).

2.SM.3.2 Comparison of Trend Slope Calculation Methods

We would like to fit a straight line to a given time series of observations $\{y_i\}$ that correspond to an independent variable (instants of time) $\{x_i\}$:

$$y_i = a + bx_i + e_i,\ i = 1, \cdots, N$$

where a and b are constant parameters to be determined, while $\{e_i\}$ represents residual variability in observations (with regard to the straight line $y = a + bx$). Without any additional assumptions, one can find the least squares solution for the trend line, that is, $\hat{a}$ and $\hat{b}$ that minimizes the overall squared error $\sum_1^N e_i^2$ in the equation above:

$$\hat{b} = \frac{\sum_{i=1}^{N}(x_i - m_x)(y_i - m_y)}{\sum_{i=1}^{N}(x_i - m_x)^2},\ \hat{a} = m_y - \hat{b}m_x \qquad (2.SM.1)$$

where m_x and m_y are sample means of x and y, respectively:

$$m_x = \frac{1}{N}\sum_{i=1}^{N} x_i,\ m_y = \frac{1}{N}\sum_{i=1}^{N} y_i \qquad (2.SM.2)$$

Data residuals (or errors in the linear fit) are

$$\hat{e}_i = y_i - (\hat{a} + \hat{b}x_i),\ i = 1, \cdots, N \qquad (2.SM.3)$$

To estimate uncertainty in $\hat{a}$ and $\hat{b}$, it is useful to view $\{e_i\}$ as a realization of some random process $\{\varepsilon_i\}$. Then the estimates of $\hat{a}$ and $\hat{b}$ can be interpreted as random variables and inferences can be made about their uncertainties, that is, deviations from their "true" values. Assumptions made about $\{\varepsilon_i\}$ affect, in general, the estimates of $\hat{a}$ and $\hat{b}$, and, usually to a larger extent, the uncertainties (confidence intervals) for these estimates.

1. Ordinary least squares (OLS) is the best known case of this kind of analysis. It assumes that all ε_i are independent identically distributed (i.i.d.) random variables with normal distribution $N(0, \sigma_e^2)$. While σ_e is usually considered unknown, in this case its unbiased estimate can be obtained from data residuals (2.SM.3) as

$$\hat{\sigma}_e^2 = \frac{1}{N-2}\sum_{i=1}^{N}\hat{e}_i^2. \qquad (2.SM.4)$$

Note that $N - 2$ appears in the denominator instead of N because two degrees of freedom out of the original N were spent on fitting two parameters a and b.

The trend slope $\hat{b}$ estimated by equation (2.SM.1) will also be normally distributed: $N(0, \sigma_b^2)$, and its standard deviation σ_b can be estimated using the σ_e estimate:

$$\hat{\sigma}_b = \hat{\sigma}_e / S_x,\quad S_x^2 = \sum_{i=1}^{N}(x_i - m_x)^2. \qquad (2.SM.5)$$

Under the assumptions made about ε_i, the random variable defined as

$$U = \frac{\hat{b} - b}{\hat{\sigma}_b}$$

has a known probability distribution, a Student's t with $N - 2$ degrees of freedom. To form a confidence interval for $\hat{b}$ such that it contains the true value of b with probability p, define

$$q = t_{\frac{1+p}{2}}(N-2) \qquad (2.SM.6)$$

that is, the $\frac{1+p}{2}$-quantile of Student's $t(N-2)$ distribution. Random-variables with this distribution lie in the interval $(-q, q)$ with probability p. From this statement applied to U, it is inferred that the interval $(\hat{b} - q\hat{\sigma}_b, \hat{b} + q\hat{\sigma}_b)$ contains b with probability p, or, as it is usually stated,

$$\hat{b} = \hat{b} \pm q\,\hat{\sigma}_b \qquad (2.SM.7)$$

where $\hat{b}$, $\hat{\sigma}_b$, and q are given by formulas (2.SM.1) to (2.SM.6).

2. OLS with reduced number of degrees of freedom by Santer et al. (2008), hereafter **S2008**. The standard OLS assumption about independence of the residual deviations of data from the straight line is often unrealistic. A better approximation to reality is a model for serially correlated error, a.k.a. first-order autoregressive model AR(1):

$$\hat{\varepsilon}_{i+1} = \rho\varepsilon_i + \delta_i,\ i = 1, \cdots, N-1 \qquad (2.SM.8)$$

where δ_i, not ε_i, are now thought of as independent random variables. For a certain class of statistical estimation problems, this kind of data interdependence acts as if the sample size was reduced to N_r:

$$N_r = N\frac{1-\rho}{1+\rho} \qquad (2.SM.9)$$

For example, if calculations by formulas (2.SM.1) to (2.SM.5) are carried through for a large sample with data dependency due to the AR(1)

model (2.SM.8), replacing $N - 2$ by $N_r - 2$ in the denominator of (4) results in a correct estimate of the trend error's standard deviation σ_b by formula (2.SM.5). Based on these theoretical considerations, Santer et al. (2008) employed a heuristic procedure that carries this calculation ahead using the value of ρ estimated from the sample of the OLS data residuals $\{\hat{e}_i\}$. Estimated $\hat{\rho}$ is the correlation coefficient between two $N - 1$-long subsamples lagged by one time step:

$$\hat{\rho} = \frac{S_{12}}{\sqrt{S_{11}S_{22}}}, \quad S_{12} = \sum_{i=1}^{N-1}(\hat{e}_i - m_1)(\hat{e}_{i+1} - m_2) \tag{2.SM.10}$$

$$S_{11} = \sum_{i=1}^{N-1}(\hat{e}_i - m_1)^2, \quad S_{22} = \sum_{i=2}^{N}(\hat{e}_i - m_2)^2 \tag{2.SM.11}$$

$$m_1 = \frac{1}{N-1}\sum_{i=1}^{N-1}\hat{e}_i, \qquad m_2 = \frac{1}{N-1}\sum_{i=2}^{N}\hat{e}_{i+1} \tag{2.SM.12}$$

(It is assumed that the timeseries are avalable on a uniform time grid without any gaps).

Furthermore, S2008 used $N_r - 2$ in place of $N - 2$ as a degree-of-freedom parameter for Student's t in (2.SM.6). Even though in case of AR(1) error the sampling distribution of U is not that of Student's t, S2008 have calculated confidence intervals for b using formulas (2.SM.1) to (2.SM.7), with (2.SM.4) and (2.SM.6) modified by the replacement of $N - 2$ by $N_r - 2$, with N_r computed by (2.SM.9) using ρ estimated according to (2.SM.10) to (2.SM.12). Their extensive numerical experiments suggested that this heuristic strategy results in reliable, conservative uncertainty estimates for the trend slope.

3. Generalized Least Squares (GLS). Rewrite the same problem as discussed above in matrix notation. Let $\mathbf{X} = [\mathbf{X}^0\ \mathbf{X}^1]$ be an $N \times 2$ matrix, and $\mathbf{Y}$ and $\mathbf{E}$ N-dimensional column-vectors such that

$$\mathbf{X}^0 = [1\cdots1]^T,\ \mathbf{X}^1 = [x_1\cdots x_N]^T,\ \mathbf{Y} = [y_i\cdots y_N]^T,\ \mathbf{E} = [e_1\cdots e_N]^T$$

Let also $\mathbf{c}^T = [a\ b]$. Then the linear trend estimation problem becomes

$$\mathbf{Y} = \mathbf{X}\mathbf{c} + \mathbf{E}$$

Let $\mathbf{E}$ be a random vector from the multivariate normal distribution $N(0, \mathbf{V})$, where $\mathbf{V}$ is a covariance matrix. The optimal estimator of $\mathbf{c}$ is

$$\hat{\mathbf{c}} = (\mathbf{X}^T\mathbf{V}^{-1}\mathbf{X})^{-1}\mathbf{X}^T\mathbf{V}^{-1}\mathbf{Y}$$

and the covariance matrix for $\hat{\mathbf{c}}$ is

$$\mathbf{P} = (\mathbf{X}^T\mathbf{V}^{-1}\mathbf{X})^{-1}$$

For the practical implementation of this method, $\mathbf{V}$ is unknown. Here we assume that $\mathbf{V}$ is a covariance matrix of an AR(1) process: $\mathbf{V} = (v_{ij})$, $v_{ij} = \sigma_e^2\rho^{|i-j|}$ where σ_e^2 and ρ are estimated as variance and lag-1 autocorrelation coefficient respectively from data residuals of the initial OLS fit, as described in equations (2.SM.4) and (2.SM.10) to (2.SM.12).

4. Prewhitening. First OLS is performed, and $\hat{\rho}$ is estimated as in (2.SM.10) above. Then the time series is prewhitened as

$$y_i' = \frac{y_{i+1} - \hat{\rho}y_i}{1 - \hat{\rho}}, \quad i = 1,\cdots,N-1 \tag{2.SM.13}$$

The OLS is applied to timeseries $\{y_i'\}$ and corresponding times $\{x_i, i = 1, \cdots, N - 1\}$. The prewhitening scheme (2.SM.13) does not change the value of the "true" trend coefficient b.

5. Sen–Theil trend estimator, or median slope method: Nonparametric estimate of the linear trend based on Kendall's τ, from Sen (1968). Relaxes the usual requirement of normal distribution of $\{\varepsilon_i\}$, but does assume i.i.d $\{\varepsilon_i\}$. No reduction of effective sample size is done.

6. Wang and Swail (2001) iterative method (WS2001). A method of trend calculation iterating between computing Sen–Theil trend slope for time series prewhitened as in equation (2.SM.13), computing data residuals of the original time series with regards to the line with this new slope, estimating $\hat{\rho}$ from these residuals (as in Equations (2.SM.10) to (2.SM.12)), prewhitening the original time series using this $\hat{\rho}$ value, etc. Zhang and Zwiers (2004) compared this method with other approaches, including Maximum Likelihood for linear trends with AR(1) error, and found it to perform best, especially for short time series.

Table 2.SM.3 | Trends (degrees Celsius per decade) and 90% confidence intervals for HadCRUT4 global mean annual time series for periods 1901–2011, 1901–1950 and 1951–2011 calculated by methods described in the Supplementary Material. Effective sample size N_r and lagged by one time step correlation coefficient for residuals $\hat{\rho}$ are given for methods that compute them. Note differences in the width of confidence intervals between methods that assume independence of data deviations from the straight line (OLS and Sen–Theil methods) and those that allow AR(1) dependence in the data (all other methods). Two of these methods use non-parametric trend estimation (Sen–Theil and WS2001).

Method	1901–2011			1901–1950			1951–2011		
	Trend	N_r	$\hat{\rho}$	Trend	N_r	$\hat{\rho}$	Trend	N_r	$\hat{\rho}$
OLS	0.075 ± 0.006			0.107 ± 0.016			0.107 ± 0.015		
S2008	0.075 ± 0.013	28	0.599	0.107 ± 0.026	21	0.407	0.107 ± 0.028	21	0.494
GLS	0.073 ± 0.012		0.599	0.100 ± 0.023		0.407	0.104 ± 0.025		0.494
Prewhitening	0.077 ± 0.013		0.594	0.113 ± 0.022		0.362	0.111 ± 0.026		0.488
Sen–Theil	0.075 (–0.006, +0.007)			0.113 (–0.019, +0.019)			0.109 (–0.017, +0.019)		
WS2001	0.079 (–0.014, +0.012)		0.596	0.114 (–0.026, +0.023)		0.352	0.110 (–0.028, +0.029)		0.487

2.SM.3.3 Method for Calculating Linear Trends and Their Uncertainties for General Use Within Chapter 2

The method applied in this chapter is a slight modification of the S2008 method. The sample size is not reduced ($N_r = N$), if the estimated $\hat{\rho}$ is negative. The method was also modified for use with time series where some data is missing. The formula (2.SM.9) for the effective sample size is still used. This formula was designed to give precise results for trend error when used for long time series of fully available data. In the presence of missing data (and shorter time series) this formula underestimates N_r further and thus results in wider (more conservative) confidence intervals (compared to the cases without missing data). The final procedure is as follows.

The time series of observations $\{y_i\}$ corresponds to instants of time $\{x_i, i = 1, \cdots, N\}$ that form a uniform grid. In some cases, observations y_i are missing. Formally, two sets of indices I_a and I_m are introduced that correspond to available and missing observations, respectively. Obviously, the union of the two sets includes all the possible data locations and the two sets do not intersect,

$$\{1, \cdots, N\} = I_a \cup I_m,\ I_a \cap I_m = \varnothing$$

The size of I_a is N_a.

First, OLS is performed for available observations:

$$\hat{b} = \frac{\sum_{i\in I_a}(x_i - m_x)(y_i - m_y)}{\sum_{i\in I_a}(x_i - m_x)^2}, \quad \hat{a} = m_y - \hat{b}m_x$$

where m_x and m_y are sample means of x and y over I_a, respectively:

$$m_x = \frac{1}{N_a}\sum_{i\in I_a} x_i, \quad m_y = \frac{1}{N_a}\sum_{i\in I_a} y_i$$

Data residuals (or trend line misfits) are

$$\hat{e}_i = y_i - (\hat{a} + \hat{b}x_i),\ i \in I_a$$

Lag-one correlation coefficient of $\{\hat{e}_i\}$ can be estimated over the subset of indices $I_c = \{i : i \in I_a \ \&\ (i+1) \in I_a\}$. Let N_c be the size of I_c. Then

$$\hat{\rho} = \frac{S_{12}}{\sqrt{S_{11}S_{22}}}, \quad S_{12} = \sum_{i\in I_c}(\hat{e}_i - m_1)(\hat{e}_{i+1} - m_2)$$
$$S_{11} = \sum_{i\in I_c}(\hat{e}_i - m_1)^2, \quad S_{22} = \sum_{i\in I_c}(\hat{e}_{i+1} - m_2)^2$$
$$m_1 = \frac{1}{N_c}\sum_{i\in I_c}\hat{e}_i, \quad m_2 = \frac{1}{N_c}\sum_{i\in I_c}\hat{e}_{i+1}$$

A provision is made for not raising the effective sample size if estimated $\hat{\rho}$ is negative:

$$\hat{\rho}_+ = \max(\hat{\rho}, 0)$$

The resulting $\hat{\rho}_+$ is used to obtain the effective sample size of the set of available observations:

$$N_r = N_a\frac{1-\hat{\rho}_+}{1+\hat{\rho}_+}$$

which is then used to estimate the variance of data deviations from the trend line:

$$\hat{\sigma}_e^2 = \frac{1}{N_r - 2}\sum_{i\in I_a}\hat{e}_i^2.$$

Therefore the variance of trend slope estimator is obtained:

$$\hat{\sigma}_b = \hat{\sigma}_e / S_x, \quad S_x^2 = \sum_{i\in I_a}(x_i - m_x)^2.$$

To construct a confidence interval for probability level p, let

$$q = t_{\frac{1+p}{2}}(N_r - 2)$$

be the $\frac{1+p}{2}$-quantile of Student's $t(N_r - 2)$ distribution. Finally

$$b = \hat{b} \pm q\,\hat{\sigma}_b$$

where $\hat{b}$, $\hat{\sigma}_b$, and q are given by formulas above.

2.SM.3.4 Smoothing Spline Method

An alternative approach is to estimate local trends using non-parametric trend models obtained by penalized smoothing of time series (e.g., Wahba, 1990; Wood, 2006; Section 6.7.2). The value in any year is considered to be the sum of a non-parametric smooth trend and a low-order autoregressive noise term. The trend is represented locally by cubic spline polynomials (Scinocca et al., 2010) and the smoothing parameter is estimated using REML allowing for serial correlation in the residuals.

2.SM.4 Changes in Temperature

2.SM.4.1 Change in Surface *In Situ* Observations Over Time

Observations are available for much of the global land surface starting in the mid-1800s or early 1900s. Availability is reduced in the most recent years owing in large part to international data exchange delays for monthly data summaries, although these have improved from many countries since AR4. Synoptic reports (used in reanalyses), and daily reports (used to analyse extremes) are also exchanged, and there has been no such decrease in their exchange. Non-digitized temperature records continue to be found in various country archives and are being digitized (Allan et al., 2011; Brunet and Jones, 2011). Efforts to create a single comprehensive raw digital data holding with provenance tracking and version control have advanced (Thorne et al., 2011; Lawrimore et al., 2013). Most historical sea surface temperature (SST) observations arise from ships, with buoy measurements and satellite data becoming a significant contribution in the 1980s. Digital archives such as the International Comprehensive Ocean-Atmosphere Data Set (ICOADS, currently version 2.5, Woodruff et al., 2011) are constantly augmented as paper archives are imaged and digitized (Brohan et al., 2009). Despite substantial efforts in data assembly, the total number of available SST observations and the percentage of the Earth's surface area that they cover remain very low for years before 1850 and

drop drastically during the two World Wars. The sampling of land and marine records through time which form the basis for the *in situ* land-surface air temperature (LSAT) and SST records detailed in the chapter are summarized in Figure 2.SM.2.

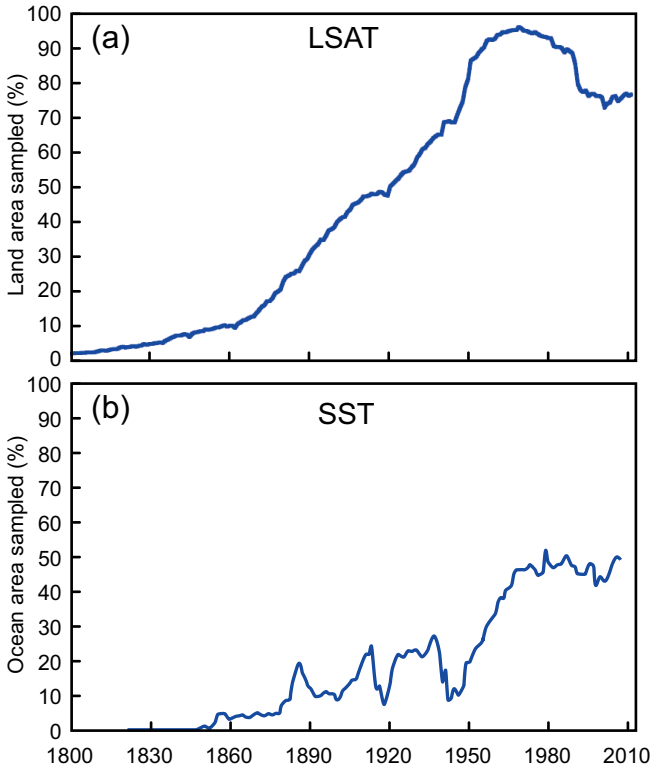

Figure 2.SM.2 | Change in percentage of possible sampled area for land records (top panel) and marine records (lower panel). Land data come from GHCNv3.2.0 and marine data from the ICOADS *in situ* record.

2.SM.4.2 Land Surface Air Temperature Data Set Innovations

Improvements have been made to the historical global data sets of land-based station observations used in AR4. Basic descriptions of the methods for the current versions of all data sets are given in Table 2.SM.4. All use monthly average temperature series from stations around the globe. Global Historical Climatology Network (GHCN) V3 improvements (Lawrimore et al., 2011) included elimination of "duplicate" time series for many stations, updating more station data with the most recent data, the application of enhanced quality assurance procedures (Durre et al., 2010) and a new pairwise homogenization approach for individual station time series (Menne and Williams, 2009). Two version increments to this V3 product to fix coding issues have since accrued that have served to slightly increase the centennial time-scale trends. Goddard Institute of Space Studies (GISS) continues to provide an estimate based primarily on GHCN but with different station inclusion criteria, additional night-light-based urban adjustments and a distinct gridding and infilling method (Hansen et al., 2010). CRUTEM4 (Jones et al., 2012) incorporates additional series above and beyond those in CRUTEM3 and also newly homogenized versions of the records for a number of stations and countries. It continues the model of incorporating the best available estimates for each station arising from research papers or individual national meteorological services with access to the best metadata on the assumption that such efforts have had most attention paid to them. In contrast, all other products considered in AR5 undertake a globally consistent homogenization processing of a given set of input data, although those data may well have been processed and adjusted at source. A new data product from a group based predominantly at Berkeley (Rohde et al., 2013) uses a kriging technique, commonly used in geostatistics, to create a global mean timeseries accounting for time-varying station biases by treating each apparently homogeneous segment as a unique record. This is substantially methodologically distinct from earlier efforts and so helps us to better explore structural uncertainty (Box 2.1) in LSAT estimates.

2.SM.4.3 Sea Surface Temperature Data Improvements and Data Set Innovations

2.SM.4.3.1 In Situ Sea Surface Temperature Data Records

Because of the irregular nature of sampling in space and time, when a large portion of observations are made from moving platforms (ships and drifting buoys), it is customary to use statistical summaries of "binned" observations (most commonly, by grid boxes) rather than individual observed values (Table 2.SM.5). Means or medians of all SST

Table 2.SM.4 | Summary of methods used by producers of global land-surface air temperature (LSAT) products. Basic methodological details are included to give a flavour of the methodological diversity. Further details can be found in the papers describing the data set construction processes cited in the text.

Dataset	Start of Record	Number of Stations	Quality Control and Homogeneity Adjustments	Infilling	Averaging Procedure
CRUTEM4 (Jones et al., 2012)	1856	5696 (4891 used in gridding)	Source specific QC and homogeneity applied generally to source data prior to collation	None	Average of the two hemispheric averages (derived by area weighted average of grid boxes) weighted 2/3 Northern Hemisphere and 1/3 Southern Hemisphere
GHCNv3 (Lawrimore et al., 2011)	1880	7280	Outlier and neighbour QC and pairwise comparison based adjustments	Limited infilling by eigenvectors (for global mean calculations only; Smith et al., 2008)	Average of grid boxes area weighted
GISS (Hansen et al., 2010)	1880	c.6300	Night lights based adjustments for urban influences	Averages to 40 large scale bins	Average of the bins with areal weighting.
Berkeley (Rohde et al., 2013)	1753	39028	Individual outliers are implicitly down-weighted. Neighbour-based test to identify breaks and each apparently homogeneous segment treated separately.	No gridding, but kriging produces field estimate based on the station constraint at each timestep.	Kriged field estimate limited to maximum 1500 km distance from any station

values in a given bin that pass quality control procedures are generally used. Standard deviations and numbers of observations in individual bins are useful for estimating uncertainties. These procedures usually serve as an initial step for producing more sophisticated gridded SST products which involve bias correction and, for "analyzed" products, interpolation and smoothing. Since AR4, many marine observations have been digitized (Brohan et al., 2009; Allan et al., 2011; Wilkinson et al., 2011), substantially improving the coverage of the latest ICOADS Release 2.5 (Woodruff et al., 2011) and of the newer data sets based on it (e.g., HadSST3, HadNMAT2).

Since AR4, major innovations have primarily been around understanding of post-1940 biases. Since 1940, ships making measurements of SST have used a variety of methods (Kent et al., 2010), each with characteristic biases (Kennedy et al., 2011a). These offsets have varied over time (Kent and Kaplan, 2006; Kent and Taylor, 2006), and for the period 2002–2007 ship SSTs are overall biased warm by 0.12°C to 0.18°C on average compared to the buoy data (Reynolds et al., 2010; Kennedy et al., 2011b, 2012). Since the 1980s, drifting and moored buoys have been producing an increasingly large fraction of global SST observations and these have tended to be colder than ship-based measurements.

Although more variable than SSTs, marine air temperatures (MATs) are assumed to be physically constrained to track SST variability because of the continuous air–sea heat exchange, at least on large spatial and temporal scales (monthly to annual, ocean basin to hemispheric). However, longer-term variations noted in some locations and periods, for example, Christy et al. (2001) and Smith and Reynolds (2002), necessitate a degree of caution. Regardless, MAT data provide a useful additional record of marine region temperature changes. Adjustments have been applied to account for the change in observing height and for the use of non-standard practices during World War II (Rayner et al., 2003) and the 19th century (Bottomley et al., 1990). Because of biases due to solar heating, only Nighttime Marine Air Temperature (NMAT) data sets have been widely used in climate analyses so far. The progress on the analytical correction of solar heating biases in recent daytime MAT data (Berry et al., 2004) allowed their use in a recent analysis (Berry and Kent, 2009). Table 2.SM.5 gives a brief description of well-known historical SST and NMAT products, organized by their type.

2.SM.4.3.2 Comparing Different Types of Data and Their Errors

Comparisons are complicated because different measurement technologies target somewhat different physical characteristics of the surface ocean. Infrared (IR) and microwave (MW) radiometers sense water temperature of the top 10 to 20 μm and 1 to 2 mm respectively, whereas *in situ* SST measurements are made in the depth range between 10 cm and several meters; these are often called "bulk" SST, with an implicit assumption that the ocean surface layer is well-mixed. This assumption is valid only for nighttime conditions or when surface winds are strong. Otherwise, the surface layer is stratified and its temperature exhibits diurnal variability (Kawai and Wada, 2007; Kennedy et al., 2007), such that measured temperature values vary with the depth and time of day of observation (Donlon et al., 2007). Aside from the diurnal variability, an independent phenomenon of a thermal skin layer takes place in the top 1 mm or so of the ocean surface and results in a strong temperature gradient across this layer (usually, cooling towards the surface) which is especially enhanced in the top 100 μm. Although all *in situ* and satellite measurements might be affected by diurnal variability, only IR satellite data are subject to the thermal skin effect. IR radiometers are said to measure "skin" temperature. Temperature at the bottom of the thermal skin layer is called "subskin temperature." MW radiometer measurements are close to this variable. To estimate error variance or to verify uncertainty estimates for SST observations by comparison of different kinds of SST data, data values have ideally to be adjusted for time and depth differences by modelling the skin effect and diurnal variability; in lieu of a model, geophysical errors are reduced by constraining the comparison to the nighttime data only which minimizes the diurnal variability effects.

Table 2.SM.5 | Data Sets of SST and NMAT Observations Used in Section 2.4.2. These data sets belong to the following categories: a database of individual *in situ* observations, gridded data sets of climate anomalies (with bucket and potentially additional bias corrections applied) and globally complete interpolated data sets based on the latter products.

Data Set	Period	Space–Time Grid Resolution	Bucket/ Bias Corrections Applied
Historical Database of In Situ Observations			
International Comprehensive Ocean – Atmosphere Data Set (ICOADS), Release 2.5 (Woodruff et al., 2011)	1662–present; 1800–present, 1960–present	Individual reports; 2° × 2° monthly summaries; 1° × 1° monthly summaries	None
Gridded Data Sets of Observed Climate Anomalies			
U.K.M.O. Hadley Centre SST, v.2 (HadSST2) (Rayner et al., 2006)	1850 – present	5° × 5° monthly	Bucket correction for pre-1941 period
U.K.M.O. Hadley Centre SST, v.3 (HadSST3) (Kennedy et al., 2011a; Kennedy et al., 2011b)	1850 – present	5° × 5° monthly	Bias correction for the entire period based on percentages of different types of observations
U.K.M.O. Hadley Centre NMAT, v.2 (HadNMAT2) (Kent et al., 2013)	1886–2010	5° × 5° monthly	Adjustments for changes in observation heights and for non-standard observing practices
Globally Complete Objective Analyses (Interpolated Products) of Historical SST Records			
U.K.M.O. Hadley Centre Interpolated SST, v.1 (HadISST) (Rayner et al., 2003)	1870 – present	1° × 1° monthly	Bucket corrections for pre-1941 period
JMA Centennial *in situ* Observation Based Estimates of SST (COBE SST) (Ishii et al., 2005)	1891 – present	1° × 1° monthly	Bucket corrections for pre-1941 period
NOAA Extended Reconstruction of SST, v. 3b (ERSSTv3b) (Smith et al., 2005, 2008)	1854 – present	2° × 2° monthly	Bucket corrections for pre-1941 period

Comparisons between *in situ* measurements and different satellite instruments have been used to assess the uncertainties in the individual measurement techniques. Random error magnitudes on Along Track Scanning Radiometer (ATSR) measurements have been estimated (O'Carroll et al., 2008; Embury et al., 2012; Kennedy et al., 2012) to lie between 0.1°C and 0.2°C. The uncertainties associated with random errors for Advanced Along Track Scanninr Radiometer (AATSR) measurements are therefore much lower than for ships (about 1°C to 1.5°C: Kent and Challenor (2006); Kent et al. (1999); Kent and Berry (2005) Reynolds et al. (2002); Kennedy et al. (2012)) or drifting buoys (0.15°C to 0.65°C: Kennedy et al. (2012); Reynolds et al. (2002); Emery et al. (2001); O'Carroll et al. (2008)).

Characterizing relative mean biases between different systems informs the procedures for homogenizing and combining different kinds of measurements. Embury et al. (2012) found average biases of less than 0.1°C between reprocessed AATSR retrievals and drifting buoy observations and of about 0.1°C between ATSR2 retrievals and buoys. Using an earlier AATSR data set, Kennedy et al. (2012) found that ship measurements were warmer relative to matched satellite SSTs than drifting buoys, suggesting ship measurements were biased relative to drifting buoy measurements by 0.18°C. They hypothesized that HadSST2 contained an increasing cool bias because of a decrease in the relative proportion of warm-biased ship observations. They applied a time-varying adjustment to the HadSST2 global means in the form of 0.18°C times the fraction of drifting buoys compared to the 1991–1995 period. This correction improved the consistency between trends in global average anomalies from the *in situ* and ATSR data sets. However, Kennedy et al. (2011b) found a smaller relative bias between ships and drifting buoys and found that changes in the biases associated with ship measurements might have been as large, or larger than, this effect.

2.SM.4.3.3 Differences in Long-Term Average Temperature Anomalies Used in Other Chapters

Figure 2.SM.3 shows the differences between selected periods that are utilized in other chapters of the report analysed in a consistent manner for those three data sets considered in Section 2.4.3. Uncertainty estimates have been calculated for HadCRUT4 using the HadCRUT4 uncertainty model (Morice et al., 2012). To allow estimates of coverage uncertainty to be made for these differences between long-term averages, HadCM3 control run fields (which are much longer) were used in place of the National centers for Environmental Prediction (NCEP) reanalysis as the globally complete reference data. It was verified that this does not greatly alter the uncertainty estimates when a subset of HadCM3 control of the same length as NCEP is used so it should not be a first-order effect.

Temperature difference between the periods of 1946-2012 and 1880-1945:

HadCRUT4:	0.38°C ± 0.04°C (90% confidence interval)
GISTEMP:	0.40°C
MLOST:	0.39°C

Temperature difference between the periods of 1986-2005 and 1850-1900:

HadCRUT4:	0.61°C ± 0.06°C (90% confidence interval)
GISTEMP:	N/A
MLOST:	N/A

Temperature difference between the periods of 2003-2012 and 1850-1900:

HadCRUT4:	0.78°C ± 0.06°C (90% confidence interval)
GISTEMP:	N/A
MLOST:	N/A

Temperature difference between the periods of 1986-2005 and 1886-1905:

HadCRUT4:	0.66°C ± 0.06°C (90% confidence interval)
GISTEMP:	0.66°C
MLOST:	0.66°C

Temperature difference between the periods of 1986-2005 and 1961-1990:

HadCRUT4:	0.30°C ± 0.03°C (90% confidence interval)
GISTEMP:	0.31°C
MLOST:	0.30°C

Temperature difference between the periods of 1986-2005 and 1980-1999:

HadCRUT4:	0.11°C ± 0.02°C (90% confidence interval)
GISTEMP:	0.11°C
MLOST:	0.11°C

2.SM.4.4 Technical Developments in Combined Land and SST Products

Table 2.SM.6 summarizes current methodological approaches. For HadCRUT4 both the land and the ocean data sources have been updated and the product now consists of 100 equi-probable solutions (Morice et al., 2012). The post-1990s period is now more consistent with the remaining products—it exhibits a greater rate of warming than the previous version over this period. NOAA's Merged Land-Ocean Surface Temperature (MLOST) analysis product has incorporated GHCNv3 and ERSST3b and reinstated high-latitude land data but is otherwise methodologically unchanged from the version considered in AR4 (Vose et al., 2012). Since AR4, NASA GISS have undertaken updates and a published sensitivity analysis focussed primarily around their urban heat island adjustments approach (Section 2.4.1.3) and choice of product and method for merging pre-satellite era and satellite era SSTs (Hansen et al., 2010). For SST several alternative data sets or combinations of data sets were considered and these choices had an impact of the order 0.04°C for the net change over the period of record. An improved concatenation of pre-satellite era and satellite era SST products removed a small apparent cooling bias in recent times. As of December 2012 GISS changed the operational SST version they used to ERSST3b. Following the release of their code the GISS method has been independently replicated in a completely different programming language (Barnes and Jones, 2011) which builds a degree of confidence in the veracity of the processing.

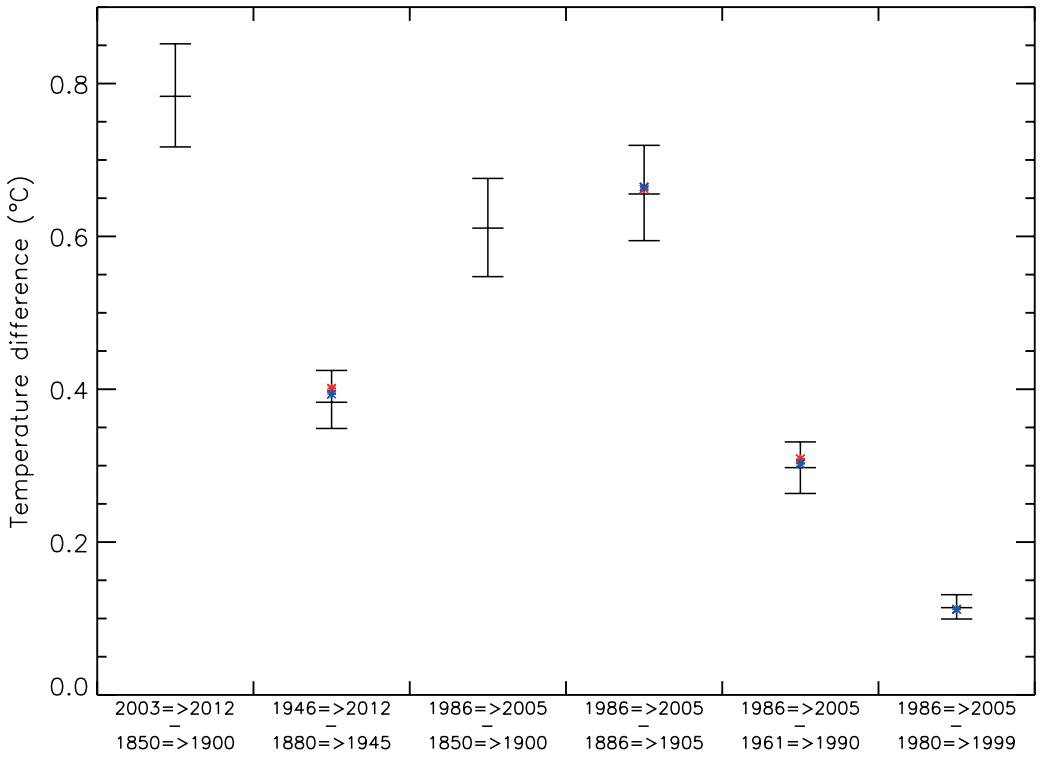

Figure 2.SM.3 | Differences in multi-year average temperatures as calculated from HadCRUT4, GISS and NCDC MLOST for six pairs of periods. The median and 5 to 95% confidence interval for differences calculated from HadCRUT4 are shown in black. Period differences for GISS are shown in red. Period differences for NCDC MLOST are shown in blue.

Table 2.SM.6 | Methodological details for the current global merged gridded surface temperature products. Only gross methodological details are included to give a flavour of the methodological diversity; further details can be found in the papers describing the data set construction processes.

Dataset	Start Date	Land Data Set	Marine Data Set	Merging of Land and Marine	Infilling	Averaging Technique
HadCRUT4 (100 versions) (Morice et al., 2012)	1850	CRUTEM4 (100 versions)	HadSST3 (100 versions)	Weighted average based on the percentage coverage	None, spatial coverage incompleteness accounted for in error model	Sum of area weighted grid box averages for Northern and Southern Hemisphere / 2
MLOST (Vose et al., 2012)	1880	GHCNv3	ERSST3b	Weighted average based on the percentage coverage	Low-frequency component filtered. Anomaly spatial covariance patterns for high-frequency component. Land and ocean interpolated separately.	Area weighted average of available gridbox values
NASA GISS (Hansen et al., 2010)	1880	GHCNv3, USHCNv2 plus Antarctic SCAR data	ERSST3b	Priority given to land data	Radius of influence up to 1200 km for land data	After gridding, non-missing values are averaged over the zones 90°S–23.6S, 23.6°S–0°, 0°–23.6°N, 23.6°N–90°N; and the four means are averaged with 3:2:2:3 weighting to represent their area.

2.SM.4.5 Technical Advances in Radiosonde Records

There now exist five estimates of radiosonde temperature evolution, which are based on a very broad range of methodological approaches to station selection, identification of artificial timeseries breaks and adjustments (Table 2.SM.7). HadAT and RATPAC were discussed in AR4 and no further technical innovations have accrued for the operational versions of these products. Development of an automated version of HadAT and discussion of efforts to characterize the resulting parametric uncertainty are summarized in the main text. A group at the University of Vienna have produced RAOBCORE and RICH (Haimberger, 2007) using ERA reanalysis products (Box 2.3) as a basis for identifying breaks. Given the relative sparseness of the observing network this may have advantageous properties in many regions compared to more traditional intra-station or neighbour-based approaches. Breakpoints are identified through reanalysis background departures using a statistical breakpoint test for both these products. Uncertainties in adjustments arising from the use of reanalyses fields to estimate the adjustments for RAOBCORE have been addressed by several variants and sensitivity studies (Haimberger, 2004, 2007; Haimberger et al., 2008).

Table 2.SM.7 | Summary of methodologies used to create the radiosonde products considered in this report. Except IUK (1960), all time series begin in 1958. Only gross methodological details are included to give a flavour of the methodological diversity; further details can be found in the papers describing the data set construction processes. Between these data set approaches a very broad range of processing choices have been considered.

Dataset	Temporal Resolution	Number of Stations	Homogeneity Test	Adjustment Method
HadAT2 (Thorne et al., 2005)	Seasonal / monthly	676	KS-test on difference series from neighbour averages together with metadata, manually interpreted	Target minus neighbour difference series based.
RATPAC (Free et al., 2005)	monthly	87	Multiple indicators and metadata assessed manually by three investigators until 1996, first difference method with *t*-test and metadata after 1995	Manually based adjustments prior to 1996, first difference derived breaks after 1995.
IUK (Sherwood et al., 2008)	Individual launch	527	Derived hierarchically looking (1) for breaks in 00Z-12Z series, (2) breaks in the series with twice daily measures, and (3) once daily ascents. Breakpoint detection was undertaken at the monthly time scale with no recourse to metadata	Relaxation to an iterative solution minimum given breaks and set of spatial and temporal basis functions.
RICH-obs (64 member ensemble) (Haimberger et al., 2012)	Individual launch	2881	SNHT test on the difference between the observed data and ERA reanalysis product background expectation field modified by metadata information.	Difference between station and a number of apparently homogeneous neighbours
RICH-tau (64 member ensemble) (Haimberger et al., 2012)	Individual launch	2881	As above	Difference between station innovation (candidate station and reanalysis background expectation field) and innovation estimates for apparently homogeneous neighbors.
RAOBCORE (Haimberger et al., 2012)	Individual launch	2881	As above	Difference between candidate station and reanalysis background expectation field

The RICH products use the same breakpoint locations but have only an indirect dependency on the reanalyses as the adjustments are neighbour based. Two varieties of RICH have been developed (Haimberger et al., 2012). The first uses pairwise neighbour difference series to estimate the required adjustment. The second uses differences in station innovations relative to the reanalyses fields. Both variants have been run in ensemble mode and the resulting uncertainty estimates are discussed in the main text. Sherwood and colleagues developed an iterative universal kriging approach for radiosonde data (Sherwood, 2007) and applied this to a global network (Sherwood et al., 2008) to create IUK (iterative universal kriging). The algorithm requires a set of break locations and the raw data and then fits an optimal estimate of the homogenized series based upon a number of basis functions including leading modes of variability. Breakpoint locations were defined by tests on the station series and without recourse to metadata.

2.SM.4.6 Advances in Microwave Sounding Unit Satellite Records

Gross methodological details of the microwave sounding unit (MSU) products are summarized in Table 2.SM.8. The University of Alabama in Huntsville (UAH) data set removed an apparent seasonal cycle artefact in the latter part of their record related to the introduction of Advanced Microwave Sounding Unit (AMSU) in version 5.3 and changed the climatological baseline to 1981–2010 to produce version 5.4. Both changes had negligible impact on trend estimates.

Version 3.2 of the RSS product (Mears and Wentz, 2009a, 2009b) for the first time incorporated a subset of AMSU instruments. It was concluded that an instantaneous correction is required to merge MSU and AMSU as they sense slightly different layers and that there will also be a systematic long-term impact unless real-world trends are vertically invariant (Mears et al., 2011). Using HadAT data this impact was estimated to be no more than 5% of the trend. Two more significant changes were accounting for latitudinal error structure dependencies, and a more physical handling of instrument body temperature effect issues in response to (Grody et al., 2004). In early 2011 version 3.3 was released which incorporated all the AMSU instruments and led to a de-emphasising of the last MSU instrument which still remained operational after 15 years, a trend reduction over the post-1998 period, and a reduction in apparent noise.

The new NOAA STAR analysis used a fundamentally distinct approach for the critical inter-satellite warm target calibration step (Zou et al., 2006). Satellites orbit in a pole-to-pole configuration with typically two satellites in operation at any time. Over most of the globe they never intersect. The exception is the polar regions where they quasi-regularly (typically once every 24 to 48 hours but this is orbital geometry dependent) sample in close proximity in space (<111 km) and time (<100 s). The STAR technique uses these Simultaneous Nadir Overpass (SNO) measures to characterize inter-satellite biases and the impact of instrument body temperature effects before accounting for diurnal drift. SNO estimates remain two point comparisons between uncertain measures over a geographically limited domain, so cannot guarantee absolute accuracy. For humidity satellite measures the geographic domain has been shown to be an issue (John et al., 2012), but it is at present unclear whether this extends to temperature measurements. Initially they produced Mid-Troposphere (MT) near-nadir measures since 1987 over the oceans (Zou et al., 2006); then included more view angles and additional channels including LS and multichannel recombinations (Zou et al., 2009); then extended back to 1979 and included land and residual instrument body temperature effects building upon the UAH methodology and diurnal corrections based upon RSS (Zou and Wang, 2010). In the latest version 2.0, STAR incorporated the AMSU observations inter-calibrated by the SNO method to extend to the present (Zou and Wang, 2011).

Table 2.SM.8 | Summary of methodologies used to create the MSU products considered in this report. All time series begin in 1978–1979. Only gross methodological details are included to give a flavour of the methodological diversity, further details can be found in the papers describing the data set construction processes.

Dataset	Inter-Satellite Calibration	Diurnal Drift Adjustments	Calibration Target Temperature Effect	MSU/AMSU Weighting Function Offsets
UAH (Christy et al., 2003)	Backbone method – adjusting all other satellites to a subset of long-lived satellites	Cross-scan differences used to infer adjustments. Measurements are adjusted to refer to the measurement time at the beginning of each satellite's mission.	Calibration target coefficients are determined as solution to system of daily equations to explain the difference between co-orbiting satellites	No accounting for differences beyond inter-satellite calibration.
RSS (Mears and Wentz, 2009a, 2009b)	Stepwise pairwise adjustments of all satellites based on difference in means. Adjustments are a function of latitude and constant in time.	Climate model output used to infer diurnal cycle. All measurements adjusted to refer to local midnight.	Values of the target temperature factors and scene temperature factors are obtained from a regression using all satellites of the same type together.	Stepwise adjustment to account for the change in weighting functions.
STAR (Zou and Wang, 2011)	Simultaneous nadir overpass measures	RSS adjustments are multiplied by a constant factor to minimize inter-satellite differences.	Largely captured in the SNO satellite intercomparison but residual artefacts are removed using the UAH method.	Channel frequency shifts on each satellite estimated and adjusted for.

2.SM.4.7 Stratospheric Sounding Unit Data Background

The Stratospheric Sounding Unit (SSU) instruments provide the only long-term near-global temperature data above the lower stratosphere, extending from the upper troposphere to the lower mesosphere (Randel et al., 2009; Seidel, 2011), with the series terminating in 2006. In theory, five channels of AMSU should be able to continue this series (Kobayashi et al., 2009) but despite incipient efforts at an AMSU-only record (Mo, 2009) and plans to merge AMSU and SSU, the current long-term series ends in 2006. The raw record has three unique additional issues to those encountered in MSU data set construction. The satellite carries a cell of CO_2 which tends to leak pressure through water egress on the ground and degassing post-launch, causing a spurious increase in observed temperatures. Compounding this the CO_2 content within the cells varies among SSU instruments (Kobayashi et al., 2009). At the higher altitudes sensed, large diurnal and semi-diurnal tides (due to absorption of solar radiation) require substantial corrections (Brownscombe et al., 1985). Finally, long-term temperature trends derived from SSU need adjustment for increasing atmospheric CO_2 (Shine et al., 2008) as this affects radiation transmission in this band.

2.SM.4.8 Global Positioning System–Radio Occultation Data Background

Global Positioning System (GPS) radio occultation (RO) fundamental observations are time delay of the occulted signal's phase traversing the atmosphere. It is based on GPS radio signals that are bent and retarded by the atmospheric refractivity field, related mainly to pressure and temperature, during their propagation to a GPS receiver on a Low Earth Orbit (LEO) satellite. An occultation event occurs whenever a GPS satellite sets (or rises from) behind the horizon and its signals are occulted by the Earth's limb. The fundamental measurement is the signal phase which is based on precise timing with atomic clocks. Potential clock errors of GPS or LEO satellites are removed by differencing methods using an additional GPS satellite as reference and by relating the measurement to even more stable oscillators on the ground. Thus, GPS RO is anchored to the international time standard and currently the only self-calibrated raw satellite measurement with SI traceability, in principle (Leroy et al., 2006; Arndt et al., 2010). Subsequent analysis converts the time delay to temperature and other parameters, which inevitably adds some degree of uncertainty to the temperature data, which is not the directly measured quantity but rather inferred with the inference being dependent on the precision of available data for other dependent parameters and how the data are processed. GPS RO measurements have several attributes that make them suited for climate studies: (1) they exhibit no satellite-to-satellite bias (Hajj et al., 2004; Ho et al., 2009a), (2) they are of very high precision (Anthes et al., 2008; Foelsche et al., 2009; Ho et al., 2009a), (3) they are not affected by clouds and precipitation, and (4) they are insensitive to retrieval error when used to estimate interannual trends in the climate system (Ho et al., 2009b). GPS–RO observations can be used to derive atmospheric temperature profiles in the upper troposphere and lower stratosphere (UT/LS) (Hajj et al., 2004; Kuo et al., 2004; Ho et al., 2009a).

2.SM.5 FAQ 2.1, Figure 2

This material documents the provenance of the data that was input to FAQ 2.1, Figure 2 in the IPCC WG1 Fifth Assessment Report. The code will also be archived at the website along with a static version of the data files when the final report is published. Two have been truncated (one marine air temperature and one sea surface temperature) for explicitly source documented and acknowledged significant issues. The FAQ includes datasets and parameters discussed in the remaining observational chapters. The data in each panel replicates that data utilized in the underlying chapters.

Land surface air temperature anomalies relative to 1961–1990:
Dark Grey: Berkeley (Rohde et al., 2013)
Green: NCDC (Lawrimore et al., 2011)
Blue: GISS (Hansen et al., 2010)
Red: CRUTEM4 (Jones et al., 2012)

Global lower tropospheric MSU-equivalent temperature anomalies relative to 1981–2010 from satellites and radiosondes.
Black : HadAT2 (Thorne et al., 2005)
Orange : RAOBCORE (Haimberger et al., 2012)
Dark Grey: RICH-obs (Haimberger et al., 2012)
Yellow: RICH-tau (Haimberger et al., 2012)
Green: RATPAC (Free et al., 2005)
Blue: RSS (Mears and Wentz, 2009a)
Red: UAH (Christy et al., 2003)

Sea-surface temperature anomalies relative to 1961–1990:
Dark Grey: ERSSTv3b (Smith et al., 2008)
Black: COBE (Ishii et al., 2005)
Green: HadISST (Rayner et al., 2006)
Red: ICOADS (Worley et al., 2005)
Yellow: HadSST3 (Kennedy et al., 2011b)

Ocean heat content anomalies (0–700 m). All data sets normalized relative to 2006–2010 and then rebased to be zero average across all data sets at 1971 as per Chapter 3, Figure 3.2.
Blue: Palmer et al. (2007)
Green: Domingues et al. (2008)
Yellow: Ishii and Kimoto (2009)
Orange: Smith and Murphy (2007)
Black: Levitus et al. (2012)

Marine air temperature anomalies relative to 1961–1990
Red: HadNMAT2 (Kent et al., 2013)
Blue: (Ishii et al., 2005). Series shown only after 1900 due to known but uncorrected biases in earlier data

Land surface specific humidity anomalies relative to 1981–2000
Green: HadCRUH (Willett et al., 2008)
Blue: (Dai, 2006)
Red: ERA Interim Reanalyses (Dee et al., 2011)
Black: HadISDH (Willett et al., 2013)

Sea level anomalies relative to 1961–1990:
Black: Church and White (2011)
Yellow: Jevrejeva et al. (2008)
Green: Ray and Douglas (2011)
Red: Nerem et al. (2010)
Orange: Ablain et al. (2009)
Blue: Leuliette and Scharroo (2010)

Northern Hemisphere March–April snow cover anomalies relative to 1967–1990
Blue: Brown (2000)
Red: Robinson and Frei (2000)
Note: Figures 4.19 and SPM-2a (green line) show a combined record of the above two data sets which includes an estimate of uncertainty (updated from Brown and Robinson, 2011).

Summer (July–August–September) average Arctic sea ice extent (absolute values)
Green: Walsh and Chapman (2001)
Blue: HadISST1.2 (Rayner et al., 2003)
Red: SMMR - SBA (Comiso and Nishio, 2008)
Black: SSM/I - NT1 (Cavalieri et al., 1984) – updated in Cavalieri and Parkinson (2012) and Parkinson and Cavalieri (2012)
Yellow: AMSR2 – ABA (Comiso and Nishio, 2008)
Orange: AMSR2 – NT2 (Markus and Cavalieri, 2000)

Glacier mass balance relative to 1961–1970.
Dark grey: Cogley area weighted as updated from (Cogley, 2009). Area weighted extrapolation from directly and geodetically measured glacire mass balances. Updated to the complete Randoph Glacier Inventory [RGI] (Arendt et al., 2012)
Green: Leclercq et al. (2011)
Blue: Marzeion et al. (2012)

2.SM.6 Changes in the Hydrological Cycle

2.SM.6.1 Precipitation Trends

Figure 2.SM.4 shows the spatial variability of long-term trends (1901–2010) and more recent trends (1951–2010) over land in annual precipitation using the climate research unit (CRU), GHCN, and GPCC data sets. Rather than absolute trends (in mm per year per decade, as in Figure 2.29) trends are calculated relative to local climatology. The spatial patterns of these trends (which can be directly compared to the trends in model precipitation reported in later chapters) are broadly similar.

2.SM.6.2 Radiosonde Humidity Data

Since AR4 there have been three distinct efforts to homogenize the tropospheric humidity records from operational radiosonde measurements (Durre et al., 2009; McCarthy et al., 2009; Dai et al., 2011) (Table 2.SM.9).

2.SM.7 Changes in Extreme Events

Although trends in extremes indices for temperature agree within uncertainty ranges (Table 2.11), note that there are differences in the way that each data set has been constructed. These include (1) using different input station networks: HadGHCND and GHCNDEX use almost identical input data, that is, from the Global Historical Climatology Network-Daily (GHCN-Daily) data set (Durre et al., 2010; Menne et al., 2012) but different averaging methods, while HadEX2 primarily

Table 2.SM.9 | Methodologically distinct aspects of the three approaches to homogenizing tropospheric humidity records from radiosondes.

Data Set	Region Considered	Time Resolution and Reporting Levels	Neighbours	First Guess[a]	Automated	Variables Homogenized
Durre et al. (2009)	NH	Monthly, mandatory and significant levels to 500 hPa	Pairwise homogenization	No	Yes	Column integrated water vapour
McCarthy et al. (2009)	NH	Monthly, mandatory levels to 300 hPa	All neighbour average, iterative	Yes	Yes	Temperature, specific humidity, relative humidity
Dai et al. (2011)	Globe	Observation resolution, mandatory levels to 100 hPa	None	Yes	Yes	Dew-point depression

Notes:
[a] First guess refers to whether a manually imputed first guess for known metadata types was incorporated prior to formal homogenization efforts.

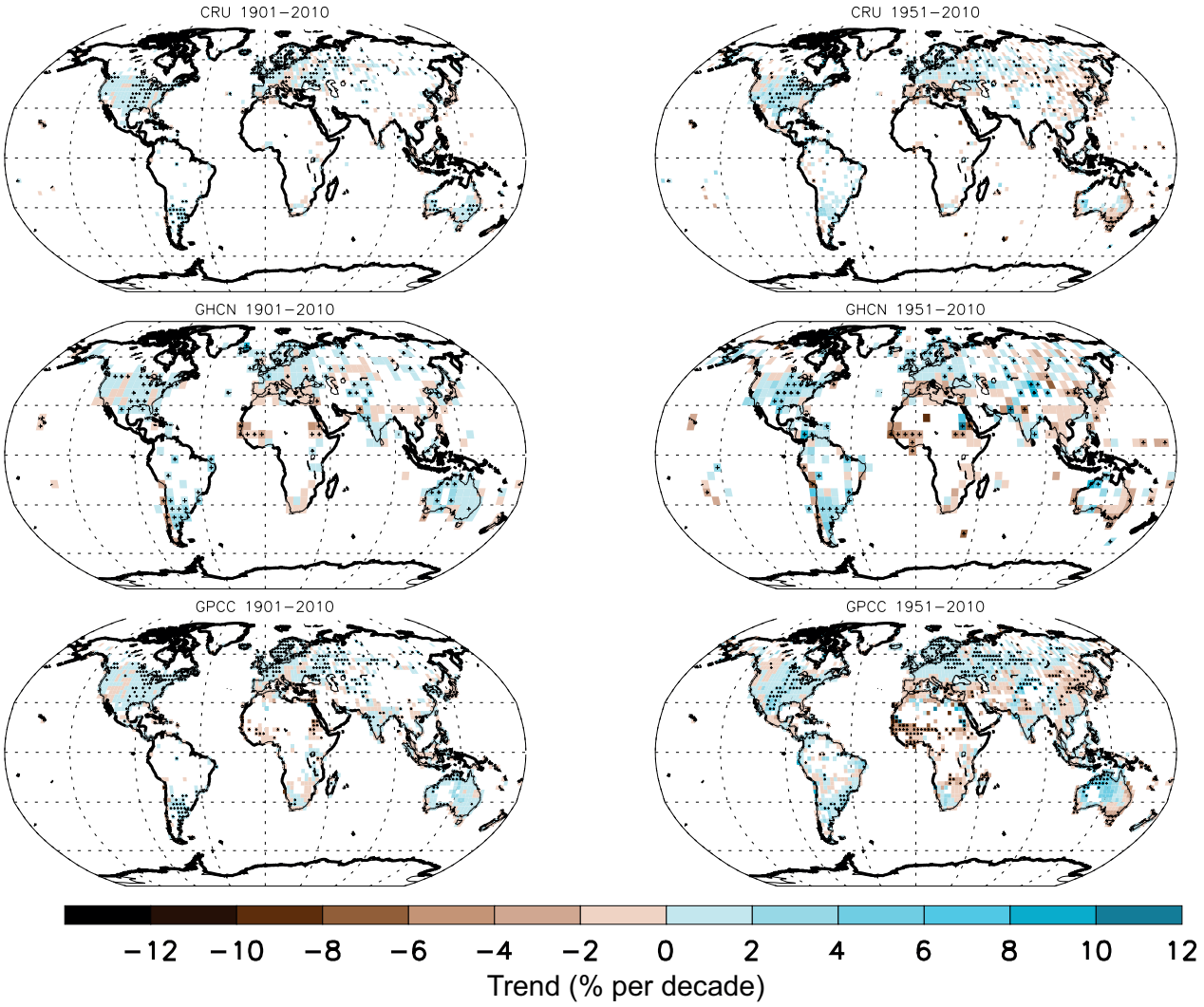

Figure 2.SM.4 | Trends in precipitation over land from the CRU, GHCN and Global Precipitation Climatology Centre (GPCC) data sets for 1901–2010 (left hand panels) and 1951–2010 (right-hand panels) as in Figure 2.29, but now in percent per decade relative to local climatology rather than in mm yr^{-1} per decade.

uses data from individual researchers or Meteororogical Services, and (2) in one case the indices are calculated from a daily gridded temperature data set (HadGHCND) while in the other two cases indices are first calculated at the station level and then gridded. This order of operation could be important to the physical interpretation of the result (Zhang et al., 2011) and its use in model evaluation for example (Chapter 9). Comparison of these three data sets presents a measure of the structural uncertainty that exists when estimating trends in global temperature extremes (Box 2.1) while still in all cases indicating a robust warming trend over the latter part of the 20th century.

A description of each data set is as follows.

2.SM.7.1 HadEX2

Unlike GHCNDEX (see later) most of the data for HadEX2 (Donat et al., 2013b) come from individual researchers or regional data sets. While HadEX2 updates a previous data set, HadEX (Alexander et al., 2006), it is not just an extension of that data set but rather represents the latest acquisition of station data. The level of quality control, however, varies from country to country. A subset of GHCN-Daily is used for the USA but whereby only selected National Weather Service Cooperative and First-Order weather observing sites with reasonably long records are used (Peterson et al., 2008) and where station time series were determined (e.g., by the statistical analysis described in Menne and Williams (2005)) to be free of significant discontinuities after 1950 caused by, e.g., changes in station location, changes in time of observation. The indices are usually pre-calculated at source before being combined into the data set using standard software (Zhang et al., 2011). In most cases the data have been carefully assessed for quality and homogeneity by researchers in the country of origin, for example, Canada (Mekis and Vincent, 2011; Vincent et al., 2012), Australia (Trewin, 2012), and where data from regional workshops were used extensive post-processing and analysis was performed (e.g., Aguilar et al., 2009; Caesar et al., 2011) to ensure data quality and homogeneity. The number of stations used in the gridding varies depending on the index being calculated (see Box 2.4, Table 1 for the types of indices calculated). For temperature indices this ranges from about 6500 to 7400 stations and for precipitation is about 11,500 stations. Data are produced on a 3.75° × 2.5° longitude/latitude grid and are available from 1901 to 2010.

2.SM.7.2 GHCNDEX

The GHCN-Daily data set (Durre et al., 2010; Menne et al., 2012) on which GHCNDEX is based currently contains about 29,000 stations with daily maximum and minimum temperature and more than 80,000 stations with daily precipitation (Donat et al., 2013a). These data have been obtained from numerous data sources that have been integrated and undergone extensive quality assurance reviews (Durre et al., 2010). Although the database is updated regularly over Europe, North America and Australia as well as at several hundred synoptic stations across numerous countries, many records from Asia, Africa and South America do not contain data from the most recent years. While many records are short or incomplete, many others, especially in North America, Europe and Australia, date back well into the 19th century. At present, however, there are no bias adjustments available for GHCN-Daily to account for historical changes in instrumentation, observing practice, station location or site conditions. Only stations with at least 40 years of valid data after 1950 are used to create GHCNDEX, as this helps to minimize the effect of varying station density. Subsequently this step reduces the number of stations used for gridding by a factor of six or seven. For example, there are approximately 4700 temperature stations for gridding the warmest maximum temperature (TXx) and about 11,500 precipitation stations for gridding the maximum one-day precipitation total (Rx1day) (see Box 2.4, Table 1 for index definitions). However, because of the criteria limiting station length, the spatial distribution of stations is confined mostly to regions outside of Africa, South America and India. Data are produced on a 2.5° × 2.5° longitude/latitude grid and are available for years from 1951 to the present.

2.SM.7.3 HadGHCND

Also uses GHCN-Daily as input (see earlier) but the order of operation is different, that is, in this case gridding of daily maximum and minimum temperatures is done first and then indices are calculated. Only temperature based indices are available. Data are produced on a 3.75° × 2.5° longitude/latitude grid and are available for years from 1951 to the present.

2.SM.8 Box 2.5: Patterns and Indices of Climate Variability

Box 2.5, Table 1 lists some prominent modes of large-scale climate variability and indices used for defining them. Further characterization including comments for each index is provided in Table 2.SM.10.

Table 2.SM.10 | Established indices of climate variability with global or regional influence. Columns are: (1) name of a climate phenomenon, (2) name of the index, (3) index definition, (4) primary references, (5) comments, including when available, characterization of the index or its spatial pattern as a dominant variability mode.

Climate Phenomenon		Index Name	Index Definition	Primary References	Characterization / Comments
El Niño – Southern Oscillation (ENSO)	Traditional indices of ENSO-related Tropical Pacific climate variability	NIÑO3	SST anomaly averaged over [5°S–5°N, 150°W–90°W]	Rasmusson and Wallace (1983), Cane (1986)	Traditional SST-based ENSO index, "devised by the Climate Analysis Center of NOAA [*now: Climate Prediction Center*] because a warming in this region strongly influences the global atmosphere" (Cane et al., 1986).
		NIÑO1	Same as above but for [10°S–5°S, 90°W–80°W]		Introduced along with NIÑO3 by NOAA's Climate Analysis Center (now: Climate Prediction Center) about 1983–1984 to describe other details of ENSO-related tropical Pacific SST variability.
		NIÑO2	Same as above but for [5°S–0°, 90°W–80°W]		
		NIÑO1+2	Same as above but for [10°S–0°, 90°W–80°W]		
		NIÑO4	Same as above but for [5°S–5°N, 160°E–150°W]		
		NIÑO3.4	Same as above but for [5°S–5°N, 170°W–120°W]	Trenberth (1997)	Used by W MO, NOAA to define El Niño/La Niña events. Detrended form is close to the first PC of linearly detrended global field of monthly SST anomalies (Deser et al., 2010)
		Troup Southern Oscillation Index (SOI)	Standardized for each calendar month SLP difference: Tahiti minus Darwin, × 10	Troup (1965)	Used by Australian Bureau of Meteorology
		SOI	Standardized difference of standardized SLP anomalies: Tahiti minus Darwin	Trenberth (1984)	Maximizes signal-to-noise ratio of linear combinations of Darwin/Tahiti records
		Darwin SOI	Standardized Darwin SLP anomaly	Trenberth and Hoar (1996)	Introduced to avoid use of the Tahiti record, considered suspicious before 1935.
		Equatorial SOI (EQSOI)	Standardized difference of standardized SLP anomalies over equatorial [5°S–5°N] Pacific Ocean: [130°W–80°W] minus [90°E–140°E]	Bell and Halpert (1998)	
	Indices of ENSO events evolution and for identifying different types of events	Trans-Niño Index (TNI)	Standardized NINO1+2 minus standardized NINO4	Trenberth and Stepaniak (2001)	Nearly uncorrelated with NINO3.4
		El Niño Modoki Index (EMI)	SSTA: [165°E–140°W, 10°S–10°N] minus ½[110°W–70°W, 15°S–5°N] minus ½[125°E–145°E, 10°S–20°N]	Ashok et al. (2007)	Defines "typical El Niño Modoki events" as those with the seasonal EMI value (JJAS or DJF means) no less than 0.7σ, where σ is the seasonal EMI standard.
		Indices of Eastern Pacific (EP) and Central Pacific (CP) types of ENSO events	EP Index: leading PC of the tropical Pacific SSTA with subtracted predictions from a linear regression on NINO4; CP index: same as EP but with NINO1+2 used in place of NINO4.	Kao and Yu (2009)	
		E and C Indices	45° orthogonal rotation of the two leading PCs of the equatorial Pacific SSTA. Approximate formulas: C = 1.7*NIÑO4 -0.1*NIÑO1+2, E = NIÑO1+2 – 0.5*NIÑO4	Takahashi et al. (2011)	Constructed to be mutually uncorrelated; many other SST-based ENSO indices are well approximated by linear combinations of E and C.
Pacific Decadal and Interdecadal Variability Intedecadal Pacific Oscillation (IPO) North Pacific Index (NPI)		Pacific Decadal Oscillation (PDO)	First PC of monthly N. Pacific SST anomaly field [20°N–70°N] with subtracted global mean; sign is selected to anti-correlate with NPI	Mantua et al. (1997); Zhang et al. (1997)	
		Projection of a global SST anomaly field onto the IPO pattern, which is found as one of the leading EOFs of a low-pass filtered global SST field; sign is selected to correlate with PDO	Folland et al. (1999); Power et al. (1999) **; Parker et al.** (2007)	IPO pattern was the third EOF for the 1911–1995 period and half power at 13.3 years; second EOF for 1891–2005 data and 11 years half power.	
		SLP [30°N–65°N; 160°E–140°W]	Trenberth and Hurrell (1994)		

(continued on next page)

Table 2.SM.10 (continued)

Climate Phenomenon		Index Name	Index Definition	Primary References	Characterization / Comments
NAO		Lisbon/ Ponta Delgada-Stykkisholmur/ Reykjavik North Atlantic Oscillation (NAO) Index	Lisbon/Ponta Delgada minus Stykkisholmur/ Reykjavik standardized SLP anomalies	Hurrell (1995)	Appears as a primary NH teleconnection pattern both in SLP and 500 hPa geopotential heigh (Z500) anomalies (Wallace and Gutzler, 1981); one of rotated PCs of NH Z700 (Barnston and Livezey, 1987). SLP anomalies can be monthly, seasonal or annual averages, resulting in the NAO index of corresponding temporal resolution (Hurrell, 1995). In Jones et al. (1997) definition, temporal averaging is applied to monthly NAO index values. NAO index is typically interpreted for boreal winter season (e.g., DJFM or NDJFM means).
		Gibraltar – South-west Iceland NAO Index	Gibraltar minus south-west Iceland / Reykjavik standardized monthly surface pressure anomalies	Jones et al. (1997)	
		PC-based NAO Index	Leading PC of SLP anomalies over the Atlantic sector [20°N–80°N, 90°W–40°E]; sign is selected to correlate with station-based NAO indices.	Hurrell (1995)	
		Summer NAO (SNAO)	Leading PC of daily SLP anomalies for July and August over the North Atlantic region [25°N–70°N, 70°W–50°E]; sign is selected to correlate with station-based (winter) NAO indices.	Folland et al. (2009)	Calculations with daily, 10-day, or July–August mean SLP data result in the same spatial pattern "characterized by a more northerly location and smaller spatial scale than its winter counterpart."
		Model-oriented NAO index	Difference between DJF SLP averages [90°W–60°E, 20°N–55°N] minus [90°W–60°E, 55°N–90°N].	Stephenson et al. (2006)	NAO index which is less sensitive to climate models' shifts of locations of maximum variability.
Annular modes	Northern Annular Mode (NAM), a.k.a. Arctic Oscillation (AO)	PC-based NAM (AO) index	First PC of the monthly mean SLP anomalies poleward of 20°N; sign is selected to correlate with NAO indices.	Thompson and Wallace (1998, 2000)	Closely related to the NAO.
	Southern Annular Mode (SAM) a.k.a. Antarctic Oscillation (AAO),	PC-based SAM index	First PC of 850 hPa or 700 hPa height anomalies south of 20°S; sign is selected to correlate with grid-based AAO and SAM indices	Thompson and Wallace (2000)	
		Grid-based SAM index: 40°S–65°S difference	Difference between normalized zonal mean SLP at 40°S and 65°S, using gridded SLP fields	Gong and Wang (1999)	
		Grid-based SAM index: 40°S–70°S difference	Same as above but uses latitudes 40°S and 70°S	Nan and Li (2003)	
		Station-based SAM index: 40°S–65°S	Difference in normalized zonal mean SLP at 40°S and 65°S, using station data	Marshall (2003)	
Pacific/North America (PNA) atmospheric teleconnection		PNA index based on centers of action	¼[Z(20°N, 160°W) – Z(45°N, 165°W) + Z(55°N, 115°W) – Z(30°N, 85°W)], Z is the location's standardized 500 hPa geopotential height anomaly	Wallace and Gutzler (1981)	A primary NH teleconnection (Wallace and Gutzler, 1981) in SLP and in 500 hPa geopotential height anomalies (Z500); second leading rotated PC of the NH Z700 (Barnston and Livezey, 1987). CPC now uses this procedure for Z500 and provides monthly updates for the results.
		PNA from rotated PC (RPC) calculation	Amplitude of the PNA pattern in the decomposition of the 500 hPa geopotential (Z500) anomaly field into the set of leading rotated EOFs obtained from the RPCA analysis of the NH Z500 monthly anomalies; sign is selected for positive correlation with the centers of action PNA index	Barnston and Livezey (1987).	
Pacific/South America (PSA) atmospheric teleconnection		PSA1 and PSA2 mode indices (PC-based)	Second and third PCs respectively of SH 500 hPa seasonal geopotential height anomaly	Mo and Paegle (2001)	Calculation was done with NCEP-NCAR reanalysis for January 1949 to March 2000. First three PCs were explaining 20%, 13% and 11% of the total variance, respectively. There are many published variations on this procedure, involving temporal filtering, using austral winter data only, PC rotation, different variables (e.g., 200 hPa streamfunction). PSA1 is positive during El Niño events (sign-selecting convention).
		PSA index based on centers of action from the 1972-1982 El Niño events composite	[–Z(35°S, 150°W) + Z(60°S, 120°W) – Z(45°S, 60°W)], Z is the location's JJA 500 hPa geopotential height anomaly	Karoly (1989)	Approximates PSA1 of the previous definition.
		PSA index based on centers of action and La Niña response sign	–[-Z(45°S, 170°W) + Z(67.5°S, 120°W) – Z(50°S, 45°W)]/3, Z is the location's 500 hPa geopotential height anomaly	Yuan and Li (2008)	Approximates (–1)*PSA1 of the PC-based definition above.

(continued on next page)

Table 2.SM.10 (continued)

Atlantic Ocean Multi-decadal Variability		Atlantic Multidecadal Oscillation (AMO) index	10-year running mean of de-trended Atlantic mean SST anomalies [0°–70°N]	Enfield et al. (2001)	Called "virtually identical" to the smoothed leading rotated N. Atlantic PC.
		Revised AMO index	As above, but subtracts global anomaly mean (60°S–60°N) instead of de-trending	Trenberth and Shea (2006)	
Tropical Atlantic Ocean variability	Atlantic Ocean Niño Mode (AONM)	ATL3	SST anomalies averaged over [3°S–3°N, 20°W–0°]	Zebiak (1993)	Identified as the two leading PCs of detrended tropical Atlantic monthly SSTA (20°S–20°N): 38% and 25% variance respectively for HadISST1, 1900–2008 (Deser et al. 2010a).
		PC-based AONM	First PC of the detrended tropical Atlantic monthly SSTA (20°S–20°N); sign is selected to correlate with ATL3	Deser et al. (2010)	
	Tropical Atlantic Meridional Mode (AMM)	PC-based AMM Index	Second PC of the detrended tropical Atlantic monthly SSTA (20°S–20°N)		
Tropical Indian Ocean variability	Indian Ocean Basin Mode (IOBM)	Basin mean index (BMI)	SST anomalies averaged over [40°–110°E, 20°S–20°N]	Yang et al. (2007)	
		IOBM, PC-based Index	The first PC of the IO detrended SST anomalies (40°E–110° E, 20°S–20°N); sign is selected by correlation with IOB basin mean index	Deser et al. (2010)	Identified as the two leading PCs of detrended tropical Indian Ocean monthly SSTA (20°S–20°N): 39% and 12% of the variance, respectively, for HadISST1, 1900–2008 (Deser et al. 2010a).
	Indian Ocean Dipole Mode (IODM)	PC-based IODM index	The second PC of the IO detrended SST anomalies (40°E–110° E, 20°S–20°N); sign is selected to correlate with DMI		
		Dipole Mode Index (DMI)	SST anomalies difference: [50°E–70°E, 10°S–10°N)] – [90°E–110°E, 10°S–0°]	Saji et al. (1999)	

References

Ablain, M., A. Cazenave, G. Valladeau, and S. Guinehut, 2009: A new assessment of the error budget of global mean sea level rate estimated by satellite altimetry over 1993–2008. *Ocean Sci.*, **5**, 193–201.

Aguilar, E., et al., 2009: Changes in temperature and precipitation extremes in western central Africa, Guinea Conakry, and Zimbabwe, 1955–2006. *J. Geophys. Res. Atmos.*, **114,** D02115.

Alexander, L. V., et al., 2006: Global observed changes in daily climate extremes of temperature and precipitation. *J. Geophys. Res. Atmos.*, **111,** D05109.

Allan, R., P. Brohan, G. P. Compo, R. Stone, J. Luterbacher, and S. Bronnimann, 2011: The International Atmospheric Circulation Reconstructions over the Earth (ACRE) initiative. *Bull. Am. Meteorol. Soc.*, **92**, 1421-1425.

Anthes, R. A., et al., 2008: The COSMOC/FORMOSAT-3 - Mission early results. *Bull. Am. Meteorol. Soc.*, **89**, 313–+.

Arendt, A., et al., 2012: Randolph Glacier Inventory [v2.0]: A Dataset of Global Glacier Outlines. Global Land Ice Measurements from Space. Digital media. http://nsidc.org/data/docs/noaa/g01130_glacier_inventory

Arndt, D. S., M. O. Baringer, and M. R. Johnson, 2010: State of the Climate in 2009. *Bull. Am. Meteorol. Soc.*, **91**, S1–S224.

Ashok, K., S. K. Behera, S. A. Rao, H. Y. Weng, and T. Yamagata, 2007: El Niño Modoki and its possible teleconnection. *J. Geophys. Res. Oceans*, **112,** C11007.

Barnes, N., and D. Jones, 2011: Clear climate code: Rewriting legacy science software for clarity. *IEEE Software*, **28**, 36–42.

Barnston, A. G., and R. E. Livezey, 1987: Classification, seasonality and persistence of low-frequency atmospheric circulation patterns. *Mon. Weather Rev.*, **115**, 1083–1126.

Beig, G., and V. Singh, 2007: Trends in tropical tropospheric column ozone from satellite data and MOZART model. *Geophys. Res. Lett.*, **34**, L17801.

Bell, G. D., and M. S. Halpert, 1998: Climate assessment for 1997. *Bull. Am. Meteorol. Soc.*, **79**, S1–S50.

Berry, D. I., and E. C. Kent, 2009: A new air-sea interaction gridded dataset from ICOADS with uncertainty estimates. *Bull. Am. Meteor. Soc.*, **90**, 645-656.

Berry, D. I., E. C. Kent, and P. K. Taylor, 2004: An analytical model of heating errors in marine air temperatures from ships. *J. Atmos. Ocean. Technol.*, **21**, 1198–1215.

Bond, T. C., et al., 2013: Bounding the role of black carbon in the climate system: A scientific assessment. *J. Geophys. Res. Atmos.*, 118, 5380–5552.

Bottomley, M., C. K. Folland, J. Hsiung, R. E. Newell, and D. E. Parker, 1990: Global ocean surface temperature atlas "GOSTA". Meteorological Office, Bracknell, UK and Department of Earth, Atmospheric and Planetary Sciences, Massachusetts Institute of Technology, Cambridge, MA, USA, 20 pp.

Brauer, M., et al., 2012: Exposure assessment for estimation of the global burden of disease attributable to outdoor air pollution. *Environ. Sci. Technol.*, **46**, 652–660.

Brohan, P., R. Allan, J. E. Freeman, A. M. Waple, D. Wheeler, C. Wilkinson, and S. Woodruff, 2009: Marine observations of old weather. *Bull. Am. Meteorol. Soc.*, **90**, 219-230.

Brown, R. D., 2000: Northern Hemisphere snow cover variability and change, 1915–97. *J. Clim.*, **13**, 2339–2355.

Brown, R. D., and D. A. Robinson, 2011: Northern Hemisphere spring snow cover variability and change over 1922–2010 including an assessment of uncertainty. *Cryosphere*, **5**, 219–229.

Brownscombe, J. L., J. Nash, G. Vaughan, and C. F. Rogers, 1985: Solar tides in the middle atmosphere. 1. Description of satellite-observations and comparison with theoretical calculations at equinox. *Q. J. R. Meteorol. Soc.*, **111**, 677–689.

Brunet, M., and P. Jones, 2011: Data rescue initiatives: Bringing historical climate data into the 21st century. *Clim. Res.*, **47**, 29–40.

Butler, J., S. Montzka, A. Clarke, J. Lobert, and J. Elkins, 1998: Growth and distribution of halons in the atmosphere. *J. Geophys. Res. Atmos.*, **103**, 1503–1511.

Caesar, J., et al., 2011: Changes in temperature and precipitation extremes over the Indo-Pacific region from 1971 to 2005. *Int. J. Climatol.*, **31**, 791–801.

Canada, 2012: Canadian Smog Science Assessment—Highlights and Key Messages. Environment Canada and Health Canada, 64 pp.

Cane, M. A., 1986: El-Niño. *Annu. Rev. Earth Planet. Sci.*, **14**, 43–70.

Cane, M. A., S. E. Zebiak, and S. C. Dolan, 1986: Experimental forecasts of El Niño. *Nature*, **321**, 827–832.

CASTNET, 2010: Clean Air Status and Trends Network (CASTNET) 2008 Annual Report. US Environmental Protection Agency, Washington, DC, 80 pp.

Cavalieri, D. J., and C. L. Parkinson, 2012: Arctic sea ice variability and trends, 1979–2010. *Cryosphere*, **6**, 957–979.

Cavalieri, D. J., P. Gloersen, and W. J. Campbell, 1984: Determination of sea ice parameters with the Nimbus-7 SMMR. *J. Geophys. Res. Atmos.*, **89**, 5355–5369.

Christy, J. R., R. W. Spencer, W. B. Norris, W. D. Braswell, and D. E. Parker, 2003: Error estimates of version 5.0 of MSU-AMSU bulk atmospheric temperatures. *J. Atmos. Ocean. Technol.*, **20**, 613–629.

Christy, J. R., D. E. Parker, S. J. Brown, I. Macadam, M. Stendel, and W. B. Norris, 2001: Differential trends in tropical sea surface and atmospheric temperatures since 1979. *Geophys. Res. Lett.*, **28**, 183–186.

Church, J. A., and N. J. White, 2011: Sea-level rise from the late 19th to the early 21st century. *Surv. Geophys.*, **32**, 585–602.

Clain, G., et al., 2009: Tropospheric ozone climatology at two Southern Hemisphere tropical/subtropical sites (Reunion Island and Irene, South Africa) from ozonesondes, LIDAR, and in situ aircraft measurements. *Atmos. Chem. Phys.*, **9**, 1723–1734.

Cogley, J. G., 2009: Geodetic and direct mass-balance measurements: comparison and joint analysis. *Ann. Glaciol.*, **50**, 96–100.

Comiso, J. C., and F. Nishio, 2008: Trends in the sea ice cover using enhanced and compatible AMSR-E, SSM/I, and SMMR data. *J. Geophys. Res. Oceans*, **113,** C02S07.

Cooper, O. R., R. S. Gao, D. Tarasick, T. Leblanc, and C. Sweeney, 2012: Long-term ozone trends at rural ozone monitoring sites across the United States, 1990–2010. *J. Geophys. Res.*, **117,** D22307.

Cunnold, D., et al., 1997: GAGE/AGAGE measurements indicating reductions in global emissions of CCl3F and CCl2F2 in 1992–1994. *J. Geophys. Res. Atmos.*, **102**, 1259–1269.

Dai, A., 2006: Recent climatology, variability, and trends in global surface humidity. *J. Clim.*, **19**, 3589–3606.

Dai, A. G., J. H. Wang, P. W. Thorne, D. E. Parker, L. Haimberger, and X. L. L. Wang, 2011: A new approach to homogenize daily radiosonde humidity data. *J. Clim.*, **24**, 965–991.

Dee, D. P., et al., 2011: The ERA-Interim reanalysis: Configuration and performance of the data assimilation system. *Q. J. R. Meteorol. Soc.*, **137**, 553–597.

Deser, C., M. A. Alexander, S. P. Xie, and A. S. Phillips, 2010: Sea surface temperature variability: Patterns and mechanisms. *Annu. Rev. Mar. Sci.*, **2**, 115–143.

Ding, A. J., T. Wang, V. Thouret, J. P. Cammas, and P. Nedelec, 2008: Tropospheric ozone climatology over Beijing: analysis of aircraft data from the MOZAIC program. *Atmos. Chem. Phys.*, **8**, 1–13.

Dlugokencky, E., et al., 2005: Conversion of NOAA atmospheric dry air CH4 mole fractions to a gravimetrically prepared standard scale. *J. Geophys. Res. Atmos.*, **110,** D18306.

Domingues, C. M., J. A. Church, N. J. White, P. J. Gleckler, S. E. Wijffels, P. M. Barker, and J. R. Dunn, 2008: Improved estimates of upper-ocean warming and multi-decadal sea-level rise. *Nature*, **453**, 1090–1093.

Donat, M. G., L. V. Alexander, H. Yang, I. Durre, R. Vose, and J. Caesar, 2013a: Global land-based datasets for monitoring climatic extremes. *Bull. Am. Meteor. Soc.*, **94**, 997-1006.

Donat, M. G., et al., 2013b: Updated analyses of temperature and precipitation extreme indices since the beginning of the twentieth century: The HadEX2 dataset. *J. Geophys. Res. Atmos.*, **118**, 2098-2118.

Donlon, C., et al., 2007: The global ocean data assimilation experiment high-resolution sea surface temperature pilot project. *Bull. Am. Meteorol. Soc.*, **88**, 1197–1213.

Durre, I., C. N. Williams, X. G. Yin, and R. S. Vose, 2009: Radiosonde-based trends in precipitable water over the Northern Hemisphere: An update. *J. Geophys. Res. Atmos.*, **114,** D05112.

Durre, I., M. J. Menne, B. E. Gleason, T. G. Houston, and R. S. Vose, 2010: Comprehensive automated quality assurance of daily surface observations. *J. Appl. Meteorol. Climatol.*, **49**, 1615–1633.

EANET, 2011: EANET Data report on the acid deposition in the East Asian Region 2009. Acid Deposition Monitoring Network in East Asia,

Embury, O., C. J. Merchant, and G. K. Corlett, 2012: A reprocessing for Climate of Sea Surface Temperature from the Along-Track Scanning Radiometers: Preliminary validation, accounting for skin and diurnal variability. *Remote Sens. Environ.*, **116**, 62-78 .

Emery, W. J., D. J. Baldwin, P. Schlussel, and R. W. Reynolds, 2001: Accuracy of *in situ* sea surface temperatures used to calibrate infrared satellite measurements. *J. Geophys. Res. Oceans*, **106**, 2387–2405.

Enfield, D. B., A. M. Mestas-Nunez, and P. J. Trimble, 2001: The Atlantic multidecadal oscillation and its relation to rainfall and river flows in the continental US. *Geophys. Res. Lett.*, **28**, 2077–2080.

Foelsche, U., B. Pirscher, M. Borsche, G. Kirchengast, and J. Wickert, 2009: Assessing the climate monitoring utility of radio occultation data: From CHAMP to FORMOSAT-3/COSMIC. *Terres. Atmos. Ocean. Sci.*, **20**, 155–170.

Folland, C. K., D. E. Parker, A. Colman, and W. R., 1999: Large scale modes of ocean surface temperature since the late nineteenth century. In: *Beyond El Nino: Decadal and Interdecadal Climate Variability* [A. Navarra (ed.)]. Springer-Verlag, New York, NY, USA, and Heidelberg, Germany, pp. 73–102.

Folland, C. K., J. Knight, H. W. Linderholm, D. Fereday, S. Ineson, and J. W. Hurrell, 2009: The summer North Atlantic Oscillation: Past, present, and future. *J. Clim.*, **22**, 1082–1103.

Fraser, P., et al., 1996: Lifetime and emission estimates of 1,1,2–trichlorotrifluorethane (CFC-113) from daily global background observations June 1982 June 1994. *J. Geophys. Res. Atmos.*, **101**, 12585–12599.

Free, M., D. J. Seidel, J. K. Angell, J. Lanzante, I. Durre, and T. C. Peterson, 2005: Radiosonde Atmospheric Temperature Products for Assessing Climate (RATPAC): A new data set of large-area anomaly time series. *J. Geophys. Res. Atmos.*, **110,** D22101.

Gong, D. Y., and S. W. Wang, 1999: Definition of Antarctic Oscillation Index. *Geophys. Res. Lett.*, **26**, 459–462.

Granier, C., et al., 2011: Evolution of anthropogenic and biomass burning emissions of air pollutants at global and regional scales during the 1980–2010 period. *Clim. Change*, **109**, 163–190.

Greally, B., et al., 2007: Observations of 1,1-difluoroethane (HFC-152a) at AGAGE and SOGE monitoring stations in 1994–2004 and derived global and regional emission estimates. *J. Geophys. Res. Atmos.*, **112,** D06308.

Grody, N. C., K. Y. Vinnikov, M. D. Goldberg, J. T. Sullivan, and J. D. Tarpley, 2004: Calibration of multisatellite observations for climatic studies: Microwave Sounding Unit (MSU). *J. Geophys. Res. Atmos.*, **109,** D24104.

Haimberger, L., 2004: Checking the temporal homogeneity of radiosonde data in the Alpine region using ERA-40 analysis feedback data. *Meteorol. Z.*, **13**, 123–129.

Haimberger, L., 2007: Homogenization of radiosonde temperature time series using innovation statistics. *J. Clim.*, **20**, 1377–1403.

Haimberger, L., C. Tavolato, and S. Sperka, 2008: Toward elimination of the warm bias in historic radiosonde temperature records - Some new results from a comprehensive intercomparison of upper-air data. *J. Clim.*, **21**, 4587–4606.

Haimberger, L., C. Tavolato, and S. Sperka, 2012: Homogenization of the global radiosonde temperature dataset through combined comparison with reanalysis background series and neighboring stations. *J. Clim.*, **25**, 8108-8131.

Hajj, G. A., et al., 2004: CHAMP and SAC-C atmospheric occultation results and intercomparisons. *J. Geophys. Res. Atmos.*, **109,** D06109.

Hall, B., G. Dutton, and J. Elkins, 2007: The NOAA nitrous oxide standard scale for atmospheric observations. *J. Geophys. Res. Atmos.*, **112,** D09305.

Hall, B., et al., 2011: Improving measurements of SF6 for the study of atmospheric transport and emissions. *Atmos. Meas. Tech.*, **4**, 2441–2451.

Han, Y. M., et al., 2011: Comparison of elemental carbon in lake sediments measured by three different methods and 150-year pollution history in eastern China. *Environ. Sci. Technol.*, **45**, 5287–5293.

Hand, J. L., et al., 2011: IMPROVE, spatial and seasonal patterns and temporal variability of haze and its constituents in the United States, Report V, ISSN 0737-5352-87, CIRA, Fort Collins, Colorado.

Hansen, J., R. Ruedy, M. Sato, and K. Lo, 2010: Global surface temperature change. *Rev. Geophys.*, **48,** RG4004.

Helmig, D., et al., 2007: A review of surface ozone in the polar regions. *Atmos. Environ.*, **41,** 5138–5161.

Hess, P. G., and R. Zbinden, 2013: Stratospheric impact on tropospheric ozone variability and trends: 1990–2009. *Atmos. Chem. Phys.*, **13**, 649–674.

Hidy, G. M., and G. T. Pennell, 2010: Multipollutant air quality management: 2010 critical review. *J. Air Waste Manage. Assoc.*, **60,** 645–674.

Ho, S. P., M. Goldberg, Y. H. Kuo, C. Z. Zou, and W. Schreiner, 2009a: Calibration of temperature in the Lower Stratosphere from microwave measurements using COSMIC radio occultation data: Preliminary results. *Terres. Atmos. Ocean. Sci.*, **20**, 87–100.

Ho, S. P., et al., 2009b: Estimating the uncertainty of using GPS radio occultation data for climate monitoring: Intercomparison of CHAMP refractivity climate records from 2002 to 2006 from different data centers. *J. Geophys. Res. Atmos.*, **114,** D23107.

Holben, B. N., et al., 1998: AERONET—A federated instrument network and data archive for aerosol characterization. *Remote Sens. Environ.*, **66**, 1–16.

Hurrell, J. W., 1995: Decadal trends in the North Atlantic Oscillation: Regional temperatures and precipitation. *Science*, **269**, 676–679.

Ishii, M., and M. Kimoto, 2009: Reevaluation of historical ocean heat content variations with time-varying XBT and MBT depth bias corrections. *J. Oceanogr.*, **65**, 287–299.

Ishii, M., A. Shouji, S. Sugimoto, and T. Matsumoto, 2005: Objective analyses of sea-surface temperature and marine meteorological variables for the 20th century using icoads and the Kobe collection. *Int. J. Climatol.*, **25**, 865–879.

Ivy, D., et al., 2012: Atmospheric histories and growth trends of C4F10, C5F12, C6F14, C7F16 and C8F18. *Atmos. Chem. Phys.*, **12**, 4313–4325.

Jevrejeva, S., J. C. Moore, A. Grinsted, and P. L. Woodworth, 2008: Recent global sea level acceleration started over 200 years ago? *Geophys. Res. Lett.*, **35,** L08715.

John, V. O., G. Holl, S. A. Buehler, B. Candy, R. W. Saunders, and D. E. Parker, 2012: Understanding intersatellite biases of microwave humidity sounders using global simultaneous nadir overpasses. *J. Geophys. Res. Atmos.*, **117**, D02305.

Jones, P. D., T. Jonsson, and D. Wheeler, 1997: Extension to the North Atlantic Oscillation using early instrumental pressure observations from Gibraltar and south-west Iceland. *Int. J. Climatol.*, **17**, 1433–1450.

Jones, P. D., D. H. Lister, T. J. Osborn, C. Harpham, M. Salmon, and C. P. Morice, 2012: Hemispheric and large-scale land-surface air temperature variations: An extensive revision and an update to 2010. *J. Geophys. Res. Atmos.*, **117**, 29.

Kao, H. Y., and J. Y. Yu, 2009: Contrasting Eastern-Pacific and Central-Pacific Types of ENSO. *J. Clim.*, **22**, 615–632.

Karoly, D., 1989: Southern-Hemisphere circulation features associated with El Niño—Southern Oscillation events. *J. Clim.*, **2**, 1239–1252.

Kaskaoutis, D. G., S. R. P, R. Gautam, M. Sharma, P. G. Kosmopoulos, and S. N. Tripathi, 2012: Variability and trends of aerosol properties over Kanpur, northern India using AERONET data (2001–10). *Environ. Res. Lett.*, **7**, 024003.

Kawai, Y., and A. Wada, 2007: Diurnal sea surface temperature variation and its impact on the atmosphere and ocean: A review. *J. Oceanogr.*, **63**, 721–744.

Keeling, C., R. Bacastow, A. Bainbridge, C. Ekdahl, P. Guenther, L. Waterman, and J. Chin, 1976: Atmospheric carbon-dioxide variations at Mauna-Loa Observatory, Hawaii. *Tellus*, **28**, 538–551.

Kennedy, J. J., P. Brohan, and S. F. B. Tett, 2007: A global climatology of the diurnal variations in sea-surface temperature and implications for MSU temperature trends. *Geophys. Res. Lett.*, **34,** L05712.

Kennedy, J. J., N. A. Rayner, and R. O. Smith, 2012: Using AATSR data to assess the quality of in situ sea surface temperature observations for climate studies. *Remote Sens. Environ.*, **116**, 79–92.

Kennedy, J. J., N. A. Rayner, R. O. Smith, D. E. Parker, and M. Saunby, 2011a: Reassessing biases and other uncertainties in sea surface temperature observations measured in situ since 1850: 2. Biases and homogenization. *J. Geophys. Res. Atmos.*, **116**, 22.

Kennedy, J. J., N. A. Rayner, R. O. Smith, D. E. Parker, and M. Saunby, 2011a: Reassessing biases and other uncertainties in sea surface temperature observations measured in situ since 1850: 2. Biases and homogenization. *J. Geophys. Res. Atmos.*, **116**, D14104.

Kent, E. C., and D. I. Berry, 2005: Quantifying random measurement errors in voluntary observing ships' meteorological observations. *Int. J. Climatol.*, **25**, 843–856.

Kent, E. C., and P. G. Challenor, 2006: Toward estimating climatic trends in SST. Part II: Random errors. *J. Atmos. Ocean. Technol.*, **23**, 476–486.

Kent, E. C., and A. Kaplan, 2006: Toward estimating climatic trends in SST. Part III: Systematic biases. *J. Atmos. Ocean. Technol.*, **23**, 487–500.

Kent, E. C., and P. K. Taylor, 2006: Toward estimating climatic trends in SST. Part I: Methods of measurement. *J. Atmos. Ocean. Technol.*, **23**, 464–475.

Kent, E. C., P. G. Challenor, and P. K. Taylor, 1999: A statistical determination of the random observational errors present in voluntary observing ships meteorological reports. *J. Atmos. Ocean. Technol.*, **16**, 905–914.

Kent, E. C., J. J. Kennedy, D. I. Berry, and R. O. Smith, 2010: Effects of instrumentation changes on sea surface temperature measured in situ. *Clim. Change*, **1**, 718–728.

Kent, E. C., N. A. Rayner, D. I. Berry, M. Saunby, B. I. Moat, J. J. Kennedy, and D. E. Parker, 2013: Global analysis of night marine air temperature and its uncertainty since 1880, the HadNMAT2 Dataset, *J. Geophys. Res.*, **118**, 1281-1298.

Kim, D.-H., B.-J. Sohn, T. Nakajima, T. Takamura, T. Takemura, B.-C. Choi, and S.-C. Yoon, 2004: Aerosol optical properties over east Asia determined from ground-based sky radiation measurements. *J. Geophys. Res.*, **109**, D02209.

Kobayashi, S., M. Matricardi, D. Dee, and S. Uppala, 2009: Toward a consistent reanalysis of the upper stratosphere based on radiance measurements from SSU and AMSU-A. *Q. J. R. Meteorol. Soc.*, **135**, 2086–2099.

Krishna Moorthy, K., S. Suresh Babu, M. R. Manoj, and S. K. Satheesh, 2013: Buildup of aerosols over the Indian Region. *Geophys. Res. Lett.*, doi:10.1002/grl.50165, in press.

Krishna Moorthy, K., S. S. Babu, S. K. Satheesh, S. Lal, M. M. Sarin, and S. Ramachandran, 2009: Climate implications of atmospheric aerosols and trace gases: Indian Scenario, Climate Sense. World Meteorological Organisation, Geneva, Switzerland, pp. 157–160.

Kuo, Y. H., T. K. Wee, S. Sokolovskiy, C. Rocken, W. Schreiner, D. Hunt, and R. A. Anthes, 2004: Inversion and error estimation of GPS radio occultation data. *J. Meteorol. Soc. Jpn.*, **82**, 507–531.

Laube, J., et al., 2010: Accelerating growth of HFC-227ea (1,1,1,2,3,3,3-heptafluoropropane) in the atmosphere. *Atmos. Chem. Phys.*, **10**, 5903–5910.

Lawrimore, J., J. Rennie, and P. Thorne, 2013: Responding to the need for better global temperature Ddata. *EOS Trans. Am. Geophys. Union*, **94**, 61–62.

Lawrimore, J. H., M. J. Menne, B. E. Gleason, C. N. Williams, D. B. Wuertz, R. S. Vose, and J. Rennie, 2011: An overview of the Global Historical Climatology Network monthly mean temperature data set, version 3. *J. Geophys. Res. Atmos.*, **116**, D19121.

Leclercq, P. W., J. Oerlemans, and J. G. Cogley, 2011: Estimating the glacier contribution to sea-level rise for the period 1800–2005. *Surv. Geophys.*, **32**, 519–535.

Lelieveld, J., J. van Aardenne, H. Fischer, M. de Reus, J. Williams, and P. Winkler, 2004: Increasing ozone over the Atlantic Ocean. *Science*, **304**, 1483–1487.

Leroy, S. S., J. G. Anderson, and J. A. Dykema, 2006: Testing climate models using GPS radio occultation: A sensitivity analysis. *J. Geophys. Res. Atmos*, **111**, D17105.

Leuliette, E. W., and R. Scharroo, 2010: Integrating Jason-2 into a multiple-altimeter climate data record. *Mar. Geodesy*, **33**, 504–517.

Levitus, S., et al., 2012: World ocean heat content and thermosteric sea level change (0–2000 m), 1955–2010. *Geophys. Res. Lett.*, **39,** L10603.

Li, H. C., K. S. Chen, C. H. Huang, and H. K. Wang, 2010: Meteorologically adjusted long-term trend of ground-level ozone concentrations in Kaohsiung County, southern Taiwan. *Atmos. Environ.*, **44**, 3605–3608.

Lin, Y. K., T. H. Lin, and C. S.C., 2010: The changes in different ozone metrics and their implications following precursor reductions over northern Taiwan from 1994 to 2007. *Environ. Monit. Assess.*, **169**, 143–157.

Logan, J. A., et al., 2012: Changes in Ozone over Europe since 1990: analysis of ozone measurements from sondes, regular Aircraft (MOZAIC), and alpine surface sites. *J. Geophys. Res.*, **117**, D09301.

Mantua, N. J., S. R. Hare, Y. Zhang, J. M. Wallace, and R. C. Francis, 1997: A Pacific interdecadal climate oscillation with impacts on salmon production. *Bull. Am. Meteorol. Soc.*, **78**, 1069–1079.

Markus, T., and D. J. Cavalieri, 2000: An enhancement of the NASA Team sea ice algorithm. *Ieee Trans. Geosci. Remote Sens*, **38**, 1387–1398.

Marshall, G. J., 2003: Trends in the southern annular mode from observations and reanalyses. *J. Clim.*, **16**, 4134–4143.

Marzeion, B., A. H. Jarosch, and M. Hofer, 2012: Past and future sea-level change from the surface mass balance of glaciers. *Cryosphere*, **6**, 1295–1322.

McCarthy, M. P., P. W. Thorne, and H. A. Titchner, 2009: An analysis of tropospheric humidity trends from radiosondes. *J. Clim.*, **22**, 5820–5838.

Mears, C. A., and F. J. Wentz, 2009a: Construction of the Remote Sensing Systems V3.2 Atmospheric temperature records from the MSU and AMSU Microwave Sounders. *J. Atmos. Ocean. Technol.*, **26**, 1040–1056.

Mears, C. A., and F. J. Wentz, 2009b: Construction of the RSS V3.2 Lower-Tropospheric temperature dataset from the MSU and AMSU Microwave Sounders. *J. Atmos. Ocean. Technol.*, **26**, 1493–1509.

Mears, C. A., F. J. Wentz, P. Thorne, and D. Bernie, 2011: Assessing uncertainty in estimates of atmospheric temperature changes from MSU and AMSU using a Monte-Carlo estimation technique. *J. Geophys. Res. Atmos.*, **116**.

Mekis, É., and L. A. Vincent, 2011: An overview of the second generation adjusted daily precipitation dataset for trend analysis in Canada. *Atmos. Ocean*, **49**, 163–177.

Menne, M. J., and C. N. Williams, 2005: Detection of undocumented changepoints using multiple test statistics and composite reference series. *J. Clim.*, **18**, 4271–4286.

Menne, M. J., and C. N. Williams, 2009: Homogenization of temperature series via pairwise comparisons. *J. Clim.*, **22**, 1700–1717.

Menne, M. J., I. Durre, B. G. Gleason, T. G. Houston, and R. S. Vose, 2012: An overview of the Global Historical Climatology Network-Daily database. *J. Atmos. Ocean. Technol.*, **29**, 897–910.

Miller, B., R. Weiss, P. Salameh, T. Tanhua, B. Greally, J. Muhle, and P. Simmonds, 2008: Medusa: A sample preconcentration and GC/MS detector system for in situ measurements of atmospheric trace halocarbons, hydrocarbons, and sulfur compounds. *Anal. Chem.*, **80**, 1536-1545 .

Miller, B., et al., 2010: HFC-23 (CHF3) emission trend response to HCFC-22 (CHClF2) production and recent HFC-23 emission abatement measures. *Atmos. Chem. Phys.*, **10**, 7875-7890.

Ministery of Environment and Forest, G. o. I., 2009: State of Environmnet Report, India–2009. Ministery of Environment and Forest, 194 pp.

Mo, K., and J. Paegle, 2001: The Pacific-South American modes and their downstream effects. *Int. J. Climatol.*, **21**, 1211–1229.

Mo, T., 2009: A study of the NOAA-15 AMSU-A brightness temperatures from 1998 through 2007. *J. Geophys. Res. Atmos.*, **114**.

Montzka, S., B. Hall, and J. Elkins, 2009: Accelerated increases observed for hydrochlorofluorocarbons since 2004 in the global atmosphere. *Geophys. Res. Lett.*, **36**, L03804.

Montzka, S., R. Myers, J. Butler, J. Elkins, and S. Cummings, 1993: Global tropospheric distribution and calibration scale of HCFC-22. *Geophys. Res. Lett.*, **20**, 703–706.

Montzka, S., M. Krol, E. Dlugokencky, B. Hall, P. Jockel, and J. Lelieveld, 2011: Small interannual variability of global atmospheric hydroxyl. *Science*, **331**, 67-69.

Montzka, S., R. Myers, J. Butler, J. Elkins, L. Lock, A. Clarke, and A. Goldstein, 1996: Observations of HFC-134a in the remote troposphere. *Geophys. Res. Lett.*, **23**, 169–172.

Morice, C. P., J. J. Kennedy, N. A. Rayner, and P. D. Jones, 2012: Quantifying uncertainties in global and regional temperature change using an ensemble of observational estimates: The HadCRUT4 data set. *J. Geophys. Res. Atmos.*, **117**, 22.

Muhle, J., et al., 2009: Sulfuryl fluoride in the global atmosphere. *J. Geophys. Res. Atmos.*, **114**, D05306.

Muhle, J., et al., 2010: Perfluorocarbons in the global atmosphere: Tetrafluoromethane, hexafluoroethane, and octafluoropropane. *Atmos. Chem. Phys.*, **10**, 5145-5164.

Nan, S., and J. P. Li, 2003: The relationship between the summer precipitation in the Yangtze River Valley and the boreal spring Southern Hemisphere annular mode. *Geophys. Res. Lett.*, **30,** 2266.

Nerem, R. S., D. P. Chambers, C. Choe, and G. T. Mitchum, 2010: Estimating mean sea level change from the TOPEX and Jason Altimeter Missions. *Mar. Geodesy*, **33**, 435–446.

O'Carroll, A. G., J. R. Eyre, and R. W. Saunders, 2008: Three-way error analysis between AATSR, AMSR-E, and in situ sea surface temperature observations. *J. Atmos. Ocean. Technol.*, **25**, 1197–1207.

O'Doherty, S., et al., 2004: Rapid growth of hydrofluorocarbon 134a and hydrochlorofluorocarbons 141b, 142b, and 22 from Advanced Global Atmospheric Gases Experiment (AGAGE) observations at Cape Grim, Tasmania, and Mace Head, Ireland. *J. Geophys. Res. Atmos.*, **109,** D06310.

O'Doherty, S., et al., 2009: Global and regional emissions of HFC-125 (CHF2CF3) from in situ and air archive atmospheric observations at AGAGE and SOGE observatories. *J. Geophys. Res. Atmos.*, **114**, D23304.

Oltmans, S. J., et al., 2013: Recent tropospheric ozone changes—A pattern dominated by slow or no growth. *Atmos. Environ.*, **67**, 331–351.

Oram, D., et al., 2012: Long-term tropospheric trend of octafluorocyclobutane (c-C4F8 or PFC-318). *Atmos. Chem. Phys.*, **12**, 261–269.

Palmer, M. D., K. Haines, S. F. B. Tett, and T. J. Ansell, 2007: Isolating the signal of ocean global warming. *Geophys. Res. Lett.*, **34**, 6.

Parker, D., C. Folland, A. Scaife, J. Knight, A. Colman, P. Baines, and B. Dong, 2007: Decadal to multidecadal variability and the climate change background. *J. Geophys. Res. Atmos.*, **112.** D18115.

Parkinson, C. L., and D. J. Cavalieri, 2012: Antarctic Sea ice variability and trends, 1979–2010. *Cryosphere*, **6**, 871–880.

Parrish, D. D., et al., 2012: Long-term changes in lower tropospheric baseline ozone concentrations at northern mid-latitudes. *Atmos. Chem. Phys.*, **12**, 11485–11504.
Peterson, T. C., X. B. Zhang, M. Brunet-India, and J. L. Vazquez-Aguirre, 2008: Changes in North American extremes derived from daily weather data. *J. Geophys. Res. Atmos.*, **113,** D07113.
Power, S., T. Casey, C. Folland, A. Colman, and V. Mehta, 1999: Inter-decadal modulation of the impact of ENSO on Australia. *Clim. Dyn.*, **15**, 319–324.
Prather, M., and J. Hsu, 2008: NF3, the greenhouse gas missing from Kyoto. *Geophys. Res. Lett.*, 35, L12810.
Prinn, R., et al., 1990: Atmospheric emissions and trends of nitrous oxide deduced from 10 years of ALE-GAGE Data. *J. Geophys. Res.*, **95**, 18, 369–18, 385.
Prinn, R., et al., 2000: A history of chemically and radiatively important gases in air deduced from ALE/GAGE/AGAGE. *J. Geophys. Res. Atmos.*, **105**, 17751–17792.
Prinn, R., et al., 2005: Evidence for variability of atmospheric hydroxyl radicals over the past quarter century. *Geophys. Res. Lett.*, L07809.
Qu, W. J., R. Arimoto, X. Y. Zhang, C. H. Zhao, Y. Q. Wang, L. F. Sheng, and G. Fu, 2010: Spatial distribution and interannual variation of surface PM10 concentrations over eighty-six Chinese cities. *Atmos. Chem. Phys.*, **10**, 5641–5662.
Quan, J., Q. Zhang, H. He, J. Liu, M. Huang, and H. Jin, 2011: Analysis of the formation of fog and haze in North China Plain (NCP). *Atmos. Chem. Phys.*, **11**, 8205–8214.
Quinn, P. K., T. S. Bates, K. Schulz, and G. E. Shaw, 2009: Decadal trends in aerosol chemical composition at Barrow, Alaska: 1976–2008. *Atmos. Chem. Phys.*, **9**, 8883–8888.
Randel, W. J., et al., 2009: An update of observed stratospheric temperature trends. *J. Geophys. Res. Atmos.*, **114,** D02107.
Rasmusson, E. M., and J. M. Wallace, 1983: Meteorological aspects of the El Niño-Southern Oscillation. *Science*, **222**, 1195–1202.
Ray, R. D., and B. C. Douglas, 2011: Experiments in reconstructing twentieth-century sea levels. *Prog. Oceanogr.*, **91**, 496–515.
Rayner, N. A., et al., 2003: Global analyses of sea surface temperature, sea ice, and night marine air temperature since the late nineteenth century. *J. Geophys. Res. Atmos.*, **108**, 37.
Rayner, N. A., et al., 2006: Improved analyses of changes and uncertainties in sea surface temperature measured in situ sice the mid-nineteenth century: The HadSST2 dataset. *J. Clim.*, **19**, 446–469.
Reynolds, R. W., C. L. Gentemann, and G. K. Corlett, 2010: Evaluation of AATSR and TMI Satellite SST Data. *J. Clim.*, **23**, 152–165.
Reynolds, R. W., N. A. Rayner, T. M. Smith, D. C. Stokes, W. Wang, and A. M. S. Ams, 2002: *An Improved In Situ and Satellite SST Analysis, J. Climate,* **15***,* 1609-1625.
Rigby, M., et al., 2008: Renewed growth of atmospheric methane. *Geophys. Res. Lett.*, **35**, L22805.
Rigby, M., et al., 2010: History of atmospheric SF6 from 1973 to 2008. *Atmos. Chem. Phys.*, **10**, 10305-10320.
Robinson, D. A., and A. Frei, 2000: Seasonal variability of Northern Hemisphere snow extent using visible satellite data. *Prof. Geogr.*, **52**, 307–315.
Rohde, R., et al., 2013: Berkeley earth temperature averaging process. *Geoinform. Geostat. An Overview*, **1:2**, doi:10.4172/2327-4581.1000103.
Saito, T., Y. Yokouchi, A. Stohl, S. Taguchi, and H. Mukai, 2010: Large emissions of perfluorocarbons in East Asia deduced from continuous atmospheric measurements. *Environ. Sci. Technol.*, **44**, 4089–4095.
Saji, N. H., B. N. Goswami, P. N. Vinayachandran, and T. Yamagata, 1999: A dipole mode in the tropical Indian Ocean. *Nature*, **401**, 360–363.
Santer, B., et al., 2008: Consistency of modelled and observed temperature trends in the tropical troposphere. *Int. J. Climatol.*, **28**, 1703–1722.
Schnadt Poberaj, C., J. Staehelin, D. Brunner, V. Thouret, H. De Backer, and R. Stübi, 2009: Long-term changes in UT/LS ozone between the late 1970s and the 1990s deduced from the GASP and MOZAIC aircraft programs and from ozonesondes. *Atmos. Chem. Phys.*, **9**, 5343–5369.
Scinocca, J. F., D. B. Stephenson, T. C. Bailey, and J. Austin, 2010: Estimates of past and future ozone trends from multimodel simulations using a flexible smoothing spline methodology. *J. Geophys. Res. Atmos.*, **115**.
Seidel, D. J., Gillett, N. P., Lanzante, J. R., Shine, K. P., Thorne, P. W., 2011: Stratospheric temperature trends: Our evolving understanding.
SEN, P., 1968: Estimates of regression coefficient based on Kendalls tau. *J. Am. Stat. Assoc.*, **63**, 1379-1389.
Sharma, S., E. Andrews, L. A. Barrie, J. A. Ogren, and D. Lavoué, 2006: Variations and sources of the equivalent black carbon in the high Arctic revealed by long-term observations at Alert and Barrow: 1989–2003. *J. Geophys. Res.*, **111**, D14208.
Sherwood, S. C., 2007: Simultaneous detection of climate change and observing biases in a network with incomplete sampling. *J. Clim.*, **20**, 4047–4062.
Sherwood, S. C., C. L. Meyer, R. J. Allen, and H. A. Titchner, 2008: Robust tropospheric warming revealed by iteratively homogenized radiosonde data. *J. Clim.*, **21**, 5336–5350.
Shine, K. P., J. J. Barnett, and W. J. Randel, 2008: Temperature trends derived from Stratospheric Sounding Unit radiances: The effect of increasing CO_2 on the weighting function. *Geophys. Res. Lett.*, **35,** L02710.
Sickles, J. E., II, and D. S. Shadwick, 2007a: Changes in air quality and atmospheric deposition in the eastern United States: 1990–2004. *J. Geophys. Res.*, **112**, D17301.
Sickles, J. E., II, and D. S. Shadwick, 2007b: Seasonal and regional air quality and atmospheric deposition in the eastern United States. *J. Geophys. Res.*, **112**, D17302.
Simmonds, P., et al., 1998: Global trends and emission estimates of CCl4 from in situ background observations from July 1978 to June 1996. *J. Geophys. Res. Atmos.*, **103**, 31331–31331.
Smith, D. M., and J. M. Murphy, 2007: An objective ocean temperature and salinity analysis using covariances from a global climate model. *J. Geophys. Res. Oceans*, **112**, C02022.
Smith, T. M., and R. W. Reynolds, 2002: Bias corrections for historical sea surface temperatures based on marine air temperatures. *J. Clim.*, **15**, 73–87.
Smith, T. M., T. C. Peterson, J. H. Lawrimore, and R. W. Reynolds, 2005: New surface temperature analyses for climate monitoring. *Geophys. Res. Lett.*, **32,** L14712.
Smith, T. M., R. W. Reynolds, T. C. Peterson, and J. Lawrimore, 2008: Improvements to NOAA's historical merged land-ocean surface temperature analysis (1880–2006). *J. Clim.*, **21**, 2283–2296.
Stemmler, K., et al., 2007: European emissions of HFC-365mfc, a chlorine-free substitute for the foam blowing agents HCFC-141b and CFC-11. *Environ. Sci. Technol.*, **41**, 1145–1151.
Stephenson, D. B., V. Pavan, M. Collins, M. M. Junge, R. Quadrelli, and C. M. G. Participating, 2006: North Atlantic Oscillation response to transient greenhouse gas forcing and the impact on European winter climate: A CMIP2 multi-model assessment. *Clim. Dynam.*, **27,** 401-420.
Takahashi, K., A. Montecinos, K. Goubanova, and B. Dewitte, 2011: ENSO regimes: Reinterpreting the canonical and Modoki El Niño. *Geophys. Res. Lett.*, **38,** L10704.
Tarasova, O. A., I. A. Senik, M. G. Sosonkin, J. Cui, J. Staehelin, and A. S. H. Prevot, 2009: Surface ozone at the Caucasian site Kislovodsk High Mountain Station and the Swiss Alpine site Jungfraujoch: data analysis and trends (1990–2006). *Atmos. Chem. Phys.*, **9**, 4157–4175.
Thompson, D. W. J., and J. M. Wallace, 1998: The Arctic Oscillation signature in the wintertime geopotential height and temperature fields. *Geophys. Res. Lett.*, **25**, 1297–1300.
Thompson, D. W. J., and J. M. Wallace, 2000: Annular modes in the extratropical circulation. Part I: Month-to-month variability. *J. Clim.*, **13**, 1000–1016.
Thompson, T. A., et al., 2004: Halocarbons and other atmospheric trace species. *Climate Monitoring and Diagnostics Laboratory Summary Report*. NOAA CMDL, Boulder, Colorado, pp.115–135.
Thorne, P. W., D. E. Parker, S. F. B. Tett, P. D. Jones, M. McCarthy, H. Coleman, and P. Brohan, 2005: Revisiting radiosonde upper air temperatures from 1958 to 2002. *J. Geophys. Res. Atmos.*, **110**, 17.
Thorne, P. W., et al., 2011: Guiding the creation of a comprehensive surface temperature resource for 21st century climate science. *Bull. Am. Meteorol. Soc.*, **92**, 40-47.
Torseth, K., et al., 2012: Introduction to the European Monitoring and Evaluation Programme (EMEP) and observed atmospheric composition change during 1972–2009. *Atmos. Chem. Phys. Discuss.*, **12**, 1733–1820.
Trenberth, K. E., 1984: Signal versus noise in the Southern Oscillation. *Mon. Weather Rev.*, **112**, 326–332.
Trenberth, K. E., 1997: The definition of El Niño. *Bull. Am. Meteorol. Soc.*, **78**, 2771–2777.
Trenberth, K. E., and J. W. Hurrell, 1994: Decadal atmosphere-ocean variations in the Pacific. *Clim. Dyn.*, **9**, 303–319.
Trenberth, K. E., and T. J. Hoar, 1996: The 1990–1995 El Niño Southern Oscillation event: Longest on record. *Geophys. Res. Lett.*, **23**, 57–60.
Trenberth, K. E., and D. P. Stepaniak, 2001: Indices of El Niño evolution. *J. Clim.*, **14**, 1697–1701.

Trenberth, K. E., and D. J. Shea, 2006: Atlantic hurricanes and natural variability in 2005. *Geophys. Res. Lett.*, **33,** L12704.

Trewin, B., 2012: A daily homogenized temperature data set for Australia. *Int. J. Climatol*., 33, 1510-1529.

Troup, A. J., 1965: Southern Oscillation. *Q. J. R. Meteorol. Soc.*, **91**, 490–.

Vignati, E., M. Karl, M. Krol, J. Wilson, P. Stier, and F. Cavalli, 2010: Sources of uncertainties in modelling black carbon at the global scale. *Atmos. Chem. Phys.*, **10**, 2595–2611.

Vincent, L. A., X. L. L. Wang, E. J. Milewska, H. Wan, F. Yang, and V. Swail, 2012: A second generation of homogenized Canadian monthly surface air temperature for climate trend analysis. *J. Geophys. Res. Atmos.*, **117,** D18110.

Vollmer, M., S. Reimann, D. Folini, L. Porter, and L. Steele, 2006: First appearance and rapid growth of anthropogenic HFC-245fa (CHF2CH2CF3) in the atmosphere. *Geophys. Res. Lett.*, **33,** L20806.

Vollmer, M., et al., 2011: Atmospheric histories and global emissions of the anthropogenic hydrofluorocarbons HFC-365mfc, HFC-245fa, HFC-227ea, and HFC-236fa. *J. Geophys. Res. Atmos.*, **116,** D08304.

Vose, R. S., et al., 2012b: NOAA's Merged Land-Ocean Surface Temperature Analysis. *Bull. Am. Meteor. Soc.*, **93**, 1677–1685.

Wahba, G., 1990: *Spline Models for Observational Data*. Society for Industrial and Applied Mathematics, Philadelphia, PA, 169pp.

Wallace, J. M., and D. S. Gutzler, 1981: Teleconnections in the geopotential height field during the Northern Hemisphere winter. *Mon. Weather Rev.*, **109**, 784–812.

Walsh, J. E., and W. L. Chapman, 2001: 20th-century sea-ice variations from observational data. *Ann. Glaciol.,* **33**, 444–448.

Wang, B., and G. Shi, 2010: Long term trends of atmospheric absorbing and scattering optical depths over China region estimated from the routine observation data of surface solar irradiances. *J. Geophys. Res. Atmos.*, **115**, D00K28

Wang, K., R. E. Dickinson, and S. Liang, 2009a: Clear sky visibility has decreased over land globally from 1973 to 2007. *Science*, **323**, 1468–1470.

Wang, K. C., R. E. Dickinson, L. Su, and K. E. Trenberth, 2012: Contrasting trends of mass and optical properties of aerosols over the Northern Hemisphere from 1992 to 2011. *Atmos. Chem. Phys.*, **12**, 9387–9398.

Wang, T., et al., 2009b: Increasing surface ozone concentrations in the background atmosphere of Southern China, 1994–2007. *Atmos. Chem. Phys.*, **9**, 6217–6227.

Wang, X. L. L., and V. R. Swail, 2001: Changes of extreme wave heights in Northern Hemisphere oceans and related atmospheric circulation regimes. *J. Clim.*, **14**, 2204–2221.

Weiss, R., J. Muhle, P. Salameh, and C. Harth, 2008: Nitrogen trifluoride in the global atmosphere. *Geophys. Res. Lett.*, **35**, L20821.

Wilkinson, C., et al., 2011: Recovery of logbooks and international marine data: the RECLAIM project. *Int. J. Climatol.*, **31**, 968–979.

Willett, K. M., P. D. Jones, N. P. Gillett, and P. W. Thorne, 2008: Recent changes in surface humidity: Development of the HadCRUH dataset. *J. Clim.*, **21**, 5364–5383.

Willett, K. M., et al., 2013: HadISDH: An updateable land surface specific humidity product for climate monitoring. *Clim. Past*, **9**, 657–677.

WMO, 2011: Scientific assessment of ozone depletion: 2010, Global Ozone Research and Monitoring Project–Report No. 52. World Meteorological Organization, Geneva, Switzerland.

Wood, S. N., 2006: *Generalized Additive Models: An Introduction with R*. CRC/Chapman & Hall, Boca Raton, FL, USA.

Woodruff, S. D., et al., 2011: ICOADS Release 2.5: Extensions and Enhancements to the Surface Marine Meteorological Archive. *Int. J. Climatol.*, **31**, 951–967.

Worley, S. J., S. D. Woodruff, R. W. Reynolds, S. J. Lubker, and N. Lott, 2005: ICOADS release 2.1 data and products. *Int. J. Climatol.*, **25**, 823–842.

Yang, J., Q. Liu, S.-P. Xie, Z. Liu, and L. Wu, 2007: Impact of the Indian Ocean SST basin mode on the Asian summer monsoon. *Geophys. Res. Lett.*, **34,** L02708.

Yttri, K. E., et al., 2011: Transboundary particulate matter in Europe, Status Report 2011. *Co-operative Programme for Monitoring and Evaluation of the Long Range Transmission of Air Pollutants (Joint CCC, MSC-W, CEIP and CIAM report 2011)*. NILU - Chemical Coordinating Centre - CCC, http://www.nilu.no/projects/ccc/reports/.

Yuan, X., and C. Li, 2008: Climate modes in southern high latitudes and their impacts on Antarctic sea ice. *J. Geophys. Res. Oceans*, **113,** C06S91.

Zebiak, S. E., 1993: Air-sea interaction in the equatorial Atlantic region. *J. Clim.*, **6**, 1567–1568.

Zhang, X., and F. Zwiers, 2004: Comment on "Applicability of prewhitening to eliminate the influence of serial correlation on the Mann-Kendall test" by Sheng Yue and Chun Yuan Wang. *Water Resourc. Res.*, **40,** W03805.

Zhang, X., et al., 2011: Indices for monitoring changes in extremes based on daily temperature and precipitation data. *Wiley Interdis. Rev. Clim. Change*, **2**, 851-870.

Zhang, X. Y., Y. Q. Wang, T. Niu, X. C. Zhang, S. L. Gong, Y. M. Zhang, and J. Y. Sun, 2012: Atmospheric aerosol compositions in China: Spatial/temporal variability, chemical signature, regional haze distribution and comparisons with global aerosols. *Atmos. Chem. Phys.*, **12**, 779–799.

Zhang, Y., J. M. Wallace, and D. S. Battisti, 1997: ENSO-like interdecadal variability: 1900–93. *J. Clim.*, **10**, 1004-1020.

Zhao, C., and P. Tans, 2006: Estimating uncertainty of the WMO mole fraction scale for carbon dioxide in air. *J. Geophys. Res. Atmos.*, **111,** D08S09.

Zou, C. Z., and W. H. Wang, 2010: Stability of the MSU-derived atmospheric temperature trend. *J. Atmos. Ocean. Technol.*, **27**, 1960–1971.

Zou, C.-Z., and W. Wang, 2011: Intersatellite calibration of AMSU-A observations for weather and climate applications. *J. Geophys. Res. Atmos.*, D23113.

Zou, C. Z., M. Gao, and M. D. Goldberg, 2009: Error structure and atmospheric temperature trends in observations from the Microwave Sounding Unit. *J. Clim.*, **22**, 1661–1681.

Zou, C. Z., M. D. Goldberg, Z. H. Cheng, N. C. Grody, J. T. Sullivan, C. Y. Cao, and D. Tarpley, 2006: Recalibration of microwave sounding unit for climate studies using simultaneous nadir overpasses. *J. Geophys. Res. Atmos.*, **111,** D19114.